Irreversible Multielement Diffusion and the Resulting Compositional and Processing Flexibility in the Synthesis and Densification of Lithium Aluminum Lanthanum Zirconium Oxide

Alexandra C. Moy[*1,2], Robert L. Sacci[2], Matthew S. Chambers[2], Amanda L. Musgrove[2], Jeff Sakamoto*[*,3], Gabriel M. Veith*[*,2]*

1. Department of Materials Science and Engineering, University of Michigan, Ann Arbor, MI 48109, USA
2. Chemical Sciences Division, Oak Ridge National Laboratory, Oak Ridge, TN, 37831, USA
3. Materials Department, University of California, Santa Barbara, CA, 93106, USA

Corresponding Author Information (*)

moyac@ornl.gov; sakamoto@ucsb.edu; veithgm@ornl.gov

Keywords

Lithium lanthanum zirconium oxide; Li loss; Al loss; synthesis; conductivity; crucible

1. Abstract

Despite the broad interest in Al-doped lithium lanthanum zirconium oxide (LLZO), the wide range of reported ionic conductivities suggests that the effect of processing parameters on the resulting phase purity and bulk conductivity is not well understood. Here, we synthesized six separate series of LLZO with variations in Al concentration, Li excess, Li addition order, Li source, densification method, and mother powder to determine the effect on the composition, phase purity, density, and bulk conductivity. We found that a wider range of compositions (6.08-7.61 mol Li, 0.06-0.23 mol Al) than previously reported can result in cubic phase stability and that nearly all elements (Li, Al, Zr, La) are lost to the MgO crucible during calcination and sintering. The manner in which different elements are lost is affected by processing parameters. We observed that Al-doped LLZO shows great compositional flexibility in stabilizing the cubic phase, offering an explanation for the range of electrochemical performance metrics reported in the literature.

2. Introduction

Cubic phase $Li_{7-3x}Al_xLa_3Zr_2O_{12}$ (LLZO-Al) is a promising electrolyte for next-generation batteries, due to its high ionic conductivity (~0.75 mS cm^{-1}),[1] chemical stability against Li metal,[2] and high fracture strength (~100 MPa) to resist dendrite propagation.[1] The resulting interest in LLZO has led to the investigation of a large number of synthesis approaches in an effort to optimize its properties and inhibit the formation of the low conductivity tetragonal LLZO (t-

LLZO) phase. Solution-based synthesis methods, such as sol-gel,[3,4] Pechini,[5] and combustion,[6,7] utilize dissolved precursors, often nitrates, to atomically mix the metal cations before drying and calcination.[8] In typical solid-state reactions, carbonates, oxides, and hydroxide precursors are mixed by dry or wet milling.[9–11] These mixtures are calcined at high temperatures of ~750-1130 °C for at least 4 hours.[5,7,10,11] Regardless of the synthesis method, the LLZO powders are then densified by pellet pressing and sintering between 900-1230 °C and 40 minutes and 36 hours.[12] In some cases, sintering aids are introduced.[13–16] Clearly, there is a wide variety of parameters that can be changed within these three steps of mixing, calcining, and sintering, such as the reaction time and temperature, the precursor chemistry, sintering crucibles, and pressure application.

One major variable of LLZO is the composition. The importance of Al doping was discovered by *Buschmann, et al.* who found that Al from the Al_2O_3 crucibles diffuses into LLZO, stabilizes the high conductivity cubic phase, and forms a Li-Al-O sintering aid.[17] Through studies involving intentional doping to stabilize cubic phase LLZO (c-LLZO) it is now known that there is a critical concentration of vacancies necessary to achieve this cubic phase through supervalent doping (~0.4 mol of Li vacancies).[18,19] This has been demonstrated for numerous supervalent dopants to include Al substituting for Li. Since this discovery, the desire to control doping concentrations has led to a variety of strategies to avoid direct contact with an Al_2O_3 crucible through the use of mother powder,[20] coatings,[10] or replacement of the Al_2O_3 crucible all together with materials such as ZrO_2, MgO, and Pt.[19,21,22] Researchers have established the Al concentration stability window for c-LLZO to be between 0.17 to 0.4 mol per formula unit and the concentration for maximum conductivity between 0.17 to 0.32 mol.[10,23–27] At low Al content the t-LLZO phase is stabilized while higher concentrations of Al result in Al-rich secondary phases that have primarily been

observed at the grain boundaries.[5,10,26,28,29] While Al plays a key role in defining phase stability and conductivity, leading to variations in crucible selection, there is a lack of understanding of other determining factors of Al concentration.

In addition to controlling how Al is doped into the LLZO structure during sintering, perceived Li losses are generally believed to require the addition of 5-20 wt.% excess Li precursor and mother powder during sintering.[9,11,17] *Huang, et al.* qualitatively confirmed that Li loss occurs during heating of Ta substituted LLZO at 1250 °C for 2 hours through observation of the formation of Li_2O on alumina plates above the samples.[30] *Heyword, et al.* tracked the lithium deficient phase evolution in *in situ* X-ray diffraction as a proxy for Li loss and found that as the mol% Li excess increased from 10 to 20%, the Li deficient phase evolved at later temperatures (900 ºC vs. no appearance as high as 1100 ºC for 1 hour).[31] Using inductively coupled plasma mass spectroscopy, *Wang, et al.* observed as much as 99% Li loss with furnace sintered samples and <4% Li loss with ultrafast high temperature sintering in Ta-substituted LLZO with 0, 10, and 20% Li excess samples.[32] For Nb- and Ca-substituted LLZO, *Limpert, et al.* quantified Li loss of 0.5 mol and 0.17 mol during 12 hours of 900 °C calcination and 1100 °C sintering, respectively.[21] The measured losses during sintering were nearly the same when done in either MgO or Al_2O_3 crucibles (0.169 mol vs. 0.149 mol). They and *Liu, et al.*, using Ta-substituted LLZO, found that the amount of Al substitution increased as the excess Li increased from 0 to 20 wt.% when an Al_2O_3 crucible was used.[21,33] The amount of Li loss seems to be independent of excess Li amount, and the conductivity (especially grain boundary) was more favorably affected by the use of an Al_2O_3 crucible than the amount of excess Li. This suggests that indeed there is a reaction between Li and alumina that acts as both a phase stabilizer and sintering aid. For example, using excess Li and sintering in an Al_2O_3

crucible leads to an increased density from approximately 2.93 to 4.47 g cm^{-3}, which results in an increase in total ionic conductivity from 2.48 x 10^{-6} to 3.66 x 10^{-4} S cm^{-1}.[33] While Li excess is not directly correlative with improved conductivity, it is correlative with the expansion of the Al range that defines the c-LLZO stability window.[7,25] Slightly different results were found in LLZO substituted with Ga supervalent doping.[34] While *Schwab, et al.* also observed Li losses, the losses depended on Li excess amounts and sintering times; while sintering at 1175 ºC, samples without Li excess had no observable Li losses regardless of sintering time and those with 20% Li excess had Li losses ranging from 0.57 to 0.94 mol Li with sintering times of 1 to 20 hours.[34] Additionally, while they also observed Al contamination from the Al_2O_3 sintering crucible, the Al concentration with the sample was independent of the Li excess concentration, unlike the Ta, Nb, and Ca-substituted samples.[21,33,34] These facts emphasize the need to analyze the effects of Li excess on LLZO-Al specifically as a function of a variety of synthesis parameters.

The addition of too much Li can stabilize the lower conducting tetragonal polymorph. In using LLZO doped with 0.24 mol Al (nominally $Li_{6.28}Al_{0.24}La_3Zr_2O_{12}$), *Rangasamy, et al.* varied the Li concentration in the LLZO synthesis from 5.63 mol to 7.32 mol Li.[10] At 6.24 mol Li they found that the cubic phase was stable while at 5.63 mol Li, the Li deficient $La_2Zr_2O_7$ phase was detected with c-LLZO, indicating that insufficient Li was present to fully react the precursors or insufficient Li was present to account for Li losses in processing. At 7.32 mol Li, t-LLZO was stable, likely due to the high Li concentration driving Li ordering within the garnet structure. However, it is important to note that in this study the Li represented the total Li in the sample across all present phases. Similar findings were observed by *Vema, et al.* in calcined $Li_{5.92}Al_{0.36}La_3Zr_2O_{12}$.[29] Calcined samples with 10% Li excess had 15% t-LLZO while samples without Li excess had no

observable tetragonal phase.[29] *Zhang, et al.* observed a similar stability range to *Rangasamy, et al.* and found that 6.35 mol Li corresponded to optimal ionic conductivity.[10,35]

In addition to modifying the Li excess, other processing variables have been changed in an effort to control the Li concentration in the LLZO during the sintering and densification step. As early as the first paper on LLZO, mother powder has been used during the sintering step to mitigate Li losses and contamination from Al_2O_3 crucibles and has since become a common practice.[3,5–7,11,14,17,20–22,34,36] While *Cheng, et al.* and *Huang, et al.* investigated the role of different mother powders on the resulting densification, phase purity, microstructure, and conductivity of LLZO, investigations that quantify the actual Li losses prevented with and without mother powder are not known to the authors and, thus, the actual effectiveness of mother powder in preventing Li loss and crucible contamination is not known.[37,38] This knowledge is especially important when considering the material costs associated with the use of the excess powder and the role of crucible contamination in affecting the final composition and sinterability of the LLZO. In addition to improved densification, pressure-assisted densification methods, such as rapid induction hot-pressing,[10] spark plasma sintering,[39] hot isostatic pressing,[40] and field assisted sintering[41] have been pursued as pathways to both improve densification and minimize Li loss due to the significantly decreased times required for densification. However, like the role of mother powder, investigations into the effectiveness of these methods in minimizing Li losses compared to traditional sintering methods is not known to the authors, again, leaving the open question as to the effect of pressure-assisted densification on the composition of the resulting garnet.

Other unexplored effects of Li include the effect of Li source and Li excess addition timing on the final properties of the LLZO. Li precursors for LLZO are commonly Li_2CO_3 and LiOH, but also include $LiNO_3$ and Li_2O.[9,11,25,42,43] Very few works have investigated the role of the lithium source in determining the final properties and composition of the LLZO.[31,42] *Dermenci, et al.* used Gibbs free energy and enthalpy of decomposition calculations to determine LiOH to be the lowest energy and enthalpy precursor as compared to Li_2CO_3 and $LiNO_3$, leading to the assumption that it was the best option for optimized densification and conductivity.[42] In contrast, using thermogravimetric analysis, *Heywood, et al.* determined that both LiOH and $LiNO_3$ decomposed ~250 ºC below Li_2CO_3 leading to the assumption that Li_2CO_3 forms LLZO at lower temperatures, making it the ideal precursor for densification and conductivity.[31] The limited work and the contrasting results among them encourage further investigation into the role of specific precursors on the composition, conductivity, structure, and density of the final LLZO products. Additionally, while these works suggest the timing of the Li incorporation into the structure is important in determining the final product, there have been no other known works that have explicitly determined the effects of the Li excess addition timing on the LLZO properties. Of these, only *Heywood, et al.* examined this role directly and found that the addition of the Li excess before calcining was more beneficial than directly before sintering, leaving the open question as to the effect of the Li excess addition during calcination.[31] Though the Li precursor and Li addition timing can have an effect on the reaction pathway to Li stuffed LLZO, there has been little work focusing on their roles.

Here we seek to clarify the roles of processing parameters on the composition and bulk conductivity of LLZO-Al by deriving LLZO processed in MgO through six separate synthesis

series with variations in Al concentration, Li excess, Li addition order, Li source, densification method, and mother powder. We performed compositional analysis on all the cations with inductively coupled plasma optical emission spectroscopy to provide and track the composition variation as a function of synthesis step. Paired with X-ray diffraction, electrochemical impedance spectroscopy, and density measurements, we analyzed the effect of composition on phase purity, structure, conductivity, and density, leading to a more holistic analysis of the LLZO itself. These measurements combined revealed a compositional flexibility of the phase space and conductivity of cubic LLZO-Al, as well as determined the effects of MgO crucible on the resulting LLZO composition. The results illustrate the importance of evaluating composition and its resulting effect on solid electrolyte properties when fabricating batteries.

3. Materials and Methods

3.1. Synthesis

The synthesis steps and process variables are outlined in Figure 1a and b, respectively. It is referenced within this section and further explained in 4.1.1. $Li_{7-3x}Al_xLa_3Zr_2O_{12}$ samples were synthesized with nominal values of x = 0.15, 0.25, or 0.35 mol. This range was selected as it was sufficient to stabilize the cubic phase (*Ia-3d* space group) and approached the Al solubility window, between 0.17 and 0.40 mol Al (Figure 1b, "Al content"). Samples were prepared from precursors of La_2O_3 (Alfa Aesar, 99.99% purity), ZrO_2 (Thermo Scientific, 99% purity), and Al_2O_3 (Alpha Resources). The Li source was varied and was either Li_2CO_3 (Alfa Aesar, 99% purity), $LiOH{\bullet}H_2O$ (Sigma-Aldrich, ≥ 98.0%), Li_2O_2 (Alfa Aesar, 95% purity), Li_2O (Alfa Aesar, 99.5%), and $LiNO_3$ (Sigma-Aldrich) (Figure 1b, "Li source"). Precursors were combined in stoichiometric quantities with either 0 to 15 wt.% excess Li_2CO_3 or 15 mol% excess Li source (Li_2CO_3, $LiOH{\bullet}H_2O$, Li_2O_2, Li_2O, $LiNO_3$) (Figure 1a, "Li Addition 1"; Figure 1b "Li_2CO_3 excess", "Li

addition order"). Precursors were ball milled (U.S. Stoneware) (Figure 1a, first step) in ethanol with 2 mm yttria stabilized zirconia milling media in a polypropylene bottle for 20 hours then dried under infrared heat lamps for 6 hours. The resulting powders were pressed into 25.4 mm pellets using a stainless steel die (SPECAC) at 2 tons. The pellets were then placed in a magnesia crucible and calcined for 4 hours at 1000 °C in a tube furnace (STT-1700C-2.5-12, Sentrotech) under flowing dry air (Airgas) (Figure 1a, second step). The calcined pellets were then ground and sieved to pass through 200 mesh. 0 to 15 wt.% excess Li source was added to the powder and the two were ground together in a mortar and pestle for 10 minutes to mix (Figure 1a, "Li Addition 2"; Figure 1b, "Li_2CO_3 excess", "Li addition order"). The mixed powder was then pressed into 25.4 mm pellets in a stainless steel die at 2 tons then put in a magnesia crucible and calcined for 4 hours at 1000 °C in a tube furnace (Figure 1a, third step). The re-calcined pellets were then ground and sieved to pass through 200 mesh. Powders are pelletized for calcination in order to increase interfacial contact between different particles for improved diffusion and enhanced rate of solid state reaction between the mixed precursors.

The calcined powders were sintered and densified using one of two methods: pressure-free sintering and pressure-assisted rapid induction hot pressing (RIHP) (Figure 1a, fourth step; Figure 1b, "Densification"). Pressure-free sintering and densification was performed by pressing 13 mm pellets from the calcined powders using a stainless steel die (SPEX SamplePrep) at 2 tons. The pellets were placed in a magnesia crucible either directly or surrounded by its own mother powder (Figure 1b, "Mother powder"). They were then sintered in the crucible for 30 hours at 1225 ºC in a tube furnace (STT-1700C-2.5-12, Sentrotech) under flowing dry air (Airgas). Powders that were

hot-pressed were densified at 47 MPa and 1225 ºC for 40 minutes. After hot-pressing each billet (~12.7 mm in diameter, ~8 mm height) was cut into pellets (~1.0 mm thick) using a diamond saw.

3.2. Characterization – Phase Purity, Chemical, Electrochemical

3.2.1. X-Ray Diffraction (XRD)

Powder X-ray diffraction (XRD) was performed using a Rigaku SmartLab equipped with HyPiX detector and Cu radiation source with a 2:1 $K\alpha_1$:$K\alpha_2$ (λ_1 = 1.54056 Å, λ_2 = 1.54439 Å) emission profile to determine the crystalline phases present after each synthesis step and the crystalline phases present in the magnesia crucibles after sintering. Data were collected in the range of $5 \leq 2\theta \leq 90^{o}$ in 0.01º steps with a scan rate of 2º min^{-1} scan rate.

Rietveld refinement[44] was performed in order to determine the lattice parameter(s) of the LLZO phase(s) and to approximate phase purity using TOPAS Academic v7.[45] The backgrounds were modelled using a 12-fold Chebyshev polynomial. Six phases were used in the refinements: $Li_{6.4}Al_{0.2}La_3Zr_2O_{12}$ (representing cubic LLZO),[46] $Li_7La_3Zr_2O_{12}$ (representing tetragonal LLZO),[47] $La_2Zr_2O_7$,[48] Li_2ZrO_3,[49] $LaAlO_3$,[50] and $LiAlO_2$.[51] Cell parameters of each phase were allowed to refine with symmetry constraints. A single isotropic atomic displacement parameter per phase was refined and a single pseudo-Voigt Thompson-Cox-Hastings peak shape was used for all phases. Atomic occupancies and coordinates were not refined.

3.2.2. Inductively Coupled Plasma Optical Emission Spectroscopy (ICP-OES)

LLZO pellets of each composition were ground using a mortar and pestle. 11.25 mL of a 25:25:50 ratio of H_2SO_4:HNO_3:H_2O was combined with 0.75 mL of 30% H_2O_2 to digest ~36 mg of the pulverized LLZO pellet The sample powder and digesting liquids were combined in a

standard 50 mL Teflon vessel which was then placed in a microwave digestor (CEM MARS 6 Microwave) at 260 ˚C for 35 minutes.[52] The resultant contents were then diluted at a 1:5 ratio with deionized water. Compositional make-ups of the digested powders were determined via ICP-OES using an iCAP 7400 ICP-OES (Thermo Fisher Scientific). Concentrations were normalized to Zr values of 1.98 to account for Hf impurities.

3.2.3. X-Ray Photoelectron Spectroscopy (XPS)

A SPECS Enviro-ESCA utilizing a 15KV monochromatic Al X-ray source was used in ultra-high vacuum mode for the X-ray Photoelectron Spectroscopy (XPS) studies. Charge correction was performed using adventitious carbon (285.0 eV) to accommodate the charging on the MgO.

3.2.4. Electrochemical Impedance Spectroscopy (EIS)

Each pellet was sanded with 320, 500, and 1200 grit sandpaper. After sanding, Au was sputtered in Ar on each side of each pellet using a custom vacuum chamber at 30 W with a base pressure of ~$4x10^{-6}$ Torr to form electrodes. EIS was performed on a sintered sample from each composition and processing variation at room temperature. EIS measurements were taken from 7 MHz to 1 Hz using a perturbation amplitude of 50 mV. A Bio-Logic SP-300 and EC-Lab V11.43 software were used to conduct the EIS measurements. An equivalent circuit was used for modeling the data and determining the bulk resistance for each sample. All alpha values for the constant phase element of each bulk process were in the range of 0.75 to 1 and χ^2 values for the equivalent circuit fits were on the order of or less than 10^{-4}. ZView 4 software (Scribner) was used to fit the Nyquist plots and results were verified with RelaxIS3 DRT (rhd instruments). Bulk conductivity was calculated from the bulk resistance as determined from the equivalent circuit, specific specimen thickness, and the electrode area.

3.2.5. Density

Pellet densities were determined by taking an average of the thickness and diameter over three locations each to calculate the volume of the pellet. The volume was then divided into the mass of the pellet to obtain the geometric density. Obtaining density through this method allows for an understanding of the porosity, and therefore the ionic conduction pathways, throughout the pellet. When determining correlation between different measured materials properties, the Pearson correlation coefficient and the distance correlation coefficient were calculated to determine the linear and nonlinear dependences.

4. Results and Discussion

4.1. Synthesis and Processing

4.1.1. Synthesis and Processing Variations

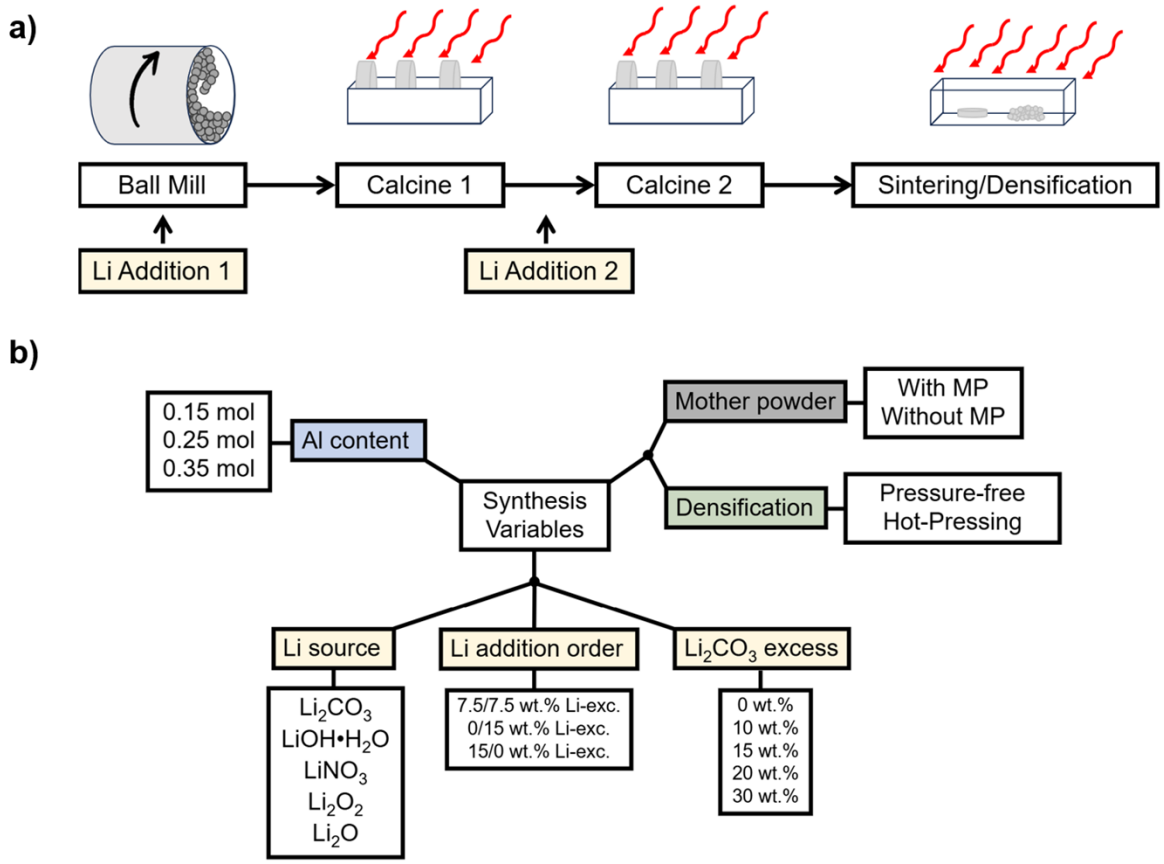

Figure 1. a) General synthesis processing flow. Labeled black squares are the major processing steps. Li addition arrows indicate where the optional Li addition steps occur. Red arrows symbolize applied heat. More red arrows indicate higher temperatures. b) Diagram depicting the different series of variables explored in this study. Boxes directly connected to the "Synthesis Variables" box identify the variable that defines each series. The white boxes connected to each of these define the specific variations of the series.

Several series of Al-doped LLZO were made to explore a variety of processing effects on the final composition, phase purity, conductivity, and density of LLZO. Each of the six series is represented in Figure 1b and are outlined in the Table of Contents of the Supporting Information

(SI). The boxes connected directly to the "Synthesis Variables" box in Figure 1b identify the variable that defines each of the series. The separate series are, "Li source," "Li_2CO_3 excess," "Li addition order," "Al content," "Mother powder," and "Densification." The variations within each series are detailed in the branching boxes and will be discussed below. There are similarities across much of the sample series. All samples follow the general synthesis steps outlined in the schematic of Figure 1a of ball milling, two calcinations, then sintering/densification. Unless otherwise stated, 0.15 mol Al is added to each sample based on recent neutron diffraction and NMR studies demonstrating ~0.17 mol Al as the minimum Al concentration needed to form a cubic garnet.[26,27,29] Where Li excess is constant, it is typically chosen to be 15 wt.% Li_2CO_3 since this is among the most common precursors and has been found to be a sufficient Li concentration for high c-LLZO phase purity in previous unpublished studies. This Li excess is then typically added in two steps, with half of it added at the "Li Addition 1" step and half in "Li Addition 2" step in Figure 1a. Two calcination steps with two Li addition steps were chosen as this improved sample purity in previous unpublished results. Sintering without pressure in mother powder is chosen as the default sintering method unless otherwise stated since it is among the most common sintering methods observed for LLZO in the literature.

The first series is the "Li source" series (Figure 1b). Five different Li precursors were used to make LLZO-Al: Li_2CO_3, $LiOH{\bullet}H_2O$, $LiNO_3$, Li_2O_2, and Li_2O. These precursors were selected as they have a wide range of melting temperatures and decomposition energies to help gain a better understanding of Li incorporation mechanisms into and reaction pathway of LLZO. Additionally, Li_2CO_3, $LiOH{\bullet}H_2O$, and $LiNO_3$ were selected as they are the most commonly used in the literature and Li_2O was selected as it is the decomposition product for those three precursors. Beyond

changing the precursor, all other processing steps were constant: across all samples Li excess was set to 15 mol% and added at the "Li addition 1" step (Figure 1a), 0.15 mol of nominal Al was used and two calcination steps and pressure-free sintering with mother powder was performed. In this case, 15 mol% Li excess was chosen rather than the typical 15 wt.% Li precursor to ensure consistent starting Li concentrations between all Li precursors.

To evaluate the role of excess Li reagent, Li excess is varied to be 0, 10, 15, 20, and 30 wt.% Li_2CO_3. All other processing steps are held constant across the tested samples. The Li excess is added in two parts: the first half is added before ball milling ("Li addition 1" in Figure 1a) and the second half is added between the two calcination steps ("Li addition 2" in Figure 1a).

To determine the effect of Li excess addition timing in the reaction pathway to LLZO, three different variations are explored for 15 wt.% Li_2CO_3 in the two step calcination synthesis: addition route 1 (7.5/7.5, "7.5/7.5 wt.% Li-exc.") corresponds to the two step addition, where half of the Li excess (7.5 wt.%) is added before the ball-milling step ("Li addition 1", Figure 1a) and the second half of the Li excess (an additional 7.5 wt.%) is added between the calcination steps ("Li addition 2", Figure 1a); addition route 2 (0/15, "0/15 wt.% Li-exc.") indicates a process where all 15 wt.% Li_2CO_3 excess is added between the calcination steps ("Li addition 2", Figure 1a); and addition route 3 (15/0, "15/0 wt.% Li-exc.") corresponds to all 15 wt.% of the Li_2CO_3 precursor excess added before the ball milling step (Figure 1a, "Li addition 1"). Li excess addition timing is explored as previous work by *Heywood, et al.* suggests that the timing of Li addition impacts the final properties of the LLZO.[31] However, they only looked at the effect of adding Li excess before

sintering and did not evaluate the effect on composition, leaving open questions as to the role of Li excess addition timing in the reaction pathway to LLZO and the final Li concentration.

The Al concentration was varied with nominal values of x = 0.15, 0.25, and 0.35 mol of Al in $Li_{7-3x}Al_xLa_3Zr_2O_{12}$ to determine the effect of Al on the resulting LLZO composition, phase purity, conductivity, and density. All other synthesis parameters were held constant: Li_2CO_3 was used as the Li precursor, the Li excess was held to 15 wt.%, a two-calcination process is used where half the Li excess is added in each of the two steps outlined in Figure 1a, and pressure-free sintering in mother powder is performed.

To determine the effect of mother powder on the phase purity, composition, conductivity, and density of LLZO and its role in preventing Li loss, LLZO-Al synthesized from several of the LLZO-Al batches above (0, 15, 30 wt.% Li excess; 0/15 and 15/0 wt.% Li excess; 15 mol% Li excess; and LLZO with intended 0.25 mol Al) were sintered with and without mother powder using Li_2CO_3 as a precursor. Pressure-free sintering was used in all cases.

Finally, we explored the effects of sintering with and without pressure on density, composition, conductivity, and phase purity. Powder synthesized with 0.15 mol nominal Al and 15 wt.% Li_2CO_3 excess, which was added in two equal Li addition steps, was sintered/densified in one of two ways. The first way was pressure-free sintering where the LLZO-Al powder was sintered in a tube furnace in mother powder at 1225 °C in flowing dry air for 30 hours, which is the standard method described above and in Figure 1a. The second method used rapid induction hot-pressing (RIHP)

at 1225 °C for 40 minutes in a flowing argon atmosphere with 47 MPa of applied pressure. Argon was needed to prevent degradation of the graphite die used for RIHP.

Given the large volume of data in this study, details of each experimentally measured lattice parameters, phase purity, composition, density, and ionic conductivity are presented in the SI. The SI table of contents summarizes these data for the reader. Figure 2 shows a representative Nyquist plot with the observed spectra (black) and the equivalent circuit fit (blue). The semicircle that is used to extrapolate the bulk conductivity is labeled in black. Representative XRD patterns, in this case, for the Li source samples, as well as the ICSD patterns for c- and t-LLZO are included for reference and are presented in Figure 3 and Figure S1.

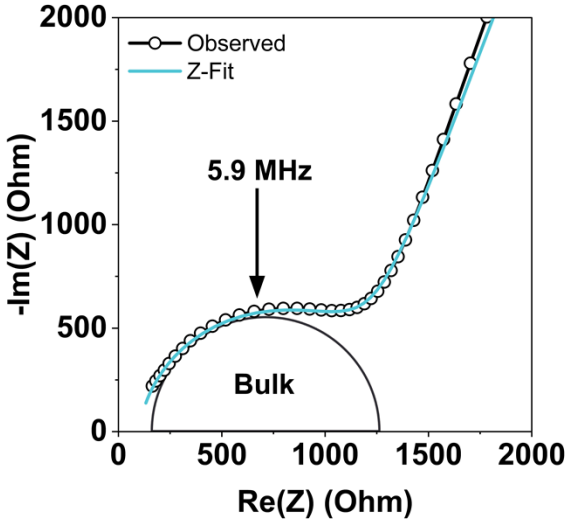

Figure 2. Nyquist plot of LLZO synthesized with $LiNO_3$ precursor at room temperature. Open black circles are the observed spectrum, and the blue line is the Z-fit. The semicircle is intended to guide the eye and indicates the bulk transport phenomenon through the grains of the LLZO. It is labeled with its characteristic frequency at the apex.

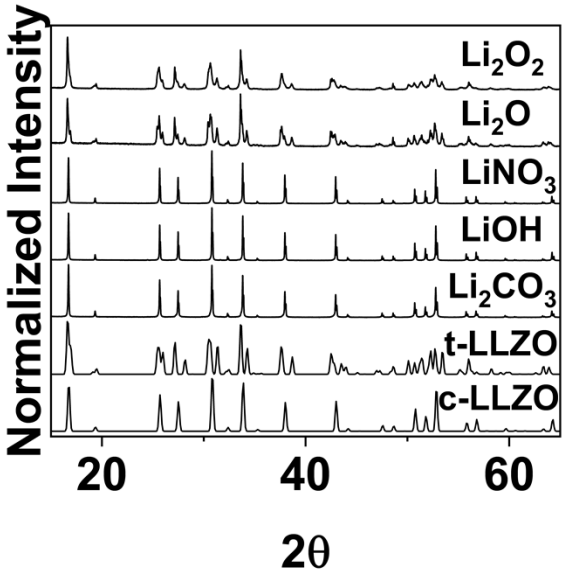

Figure 3. XRD patterns from pulverized and sintered LLZO synthesized from different precursors and ICSD standards for t-LLZO and c-LLZO. Tetragonal LLZO pattern is ICSD 246817 and cubic LLZO pattern is ICSD 195182.

4.1.2. Role of Li and Al in Determining Phase Stability and Conductivity

Figures 4 shows the correlations between experimentally measured Li and Al concentrations, phase stability, and bulk conductivity as a function of processing series where Figure 5 exclusively shows the members of each processing series with the highest measured bulk conductivity. The black symbols correspond to the ICP determined Li concentration and the red symbols correspond to the ICP determined Al concentrations as a function of bulk conductivity from the data from Figures S1-S12 and Tables S1-S12. Across nearly all samples, the LLZO phase purity as determined by XRD is greater than 98 wt.%. In previous work we have shown that, when accounting for these quantities of secondary phases, the composition of the bulk LLZO is minimally affected.[27] Additionally, previous work by *Vema, et al.* has shown the Li- and Al-rich

secondary phases detected by MAS NMR are significantly decreased and even eliminated when using increased annealing times and temperatures of 1200 ºC and 18 hours, leading to all Li and >99.1% of Al to reside in the grains of the LLZO.[29] In all cases we surpass these sintering times and temperatures: we use 1225 ºC and for all samples, except the hot-pressed sample, we sinter for 30 hours, suggesting that most, if not all, of the Li and Al reside in the structure of the LLZO itself across the samples in our study. Our processing parameters paired with our high LLZO phase purity of >98 wt.% across all samples suggests that the ICP compositions are reasonable assumptions for the bulk LLZO elemental compositions. The blue regions are the estimated tetragonal stability window as defined by the Rietveld results of the XRD performed in this study. Surprisingly, the data indicate that the tetragonal LLZO phase is stable when compositions go below ~0.06 mol of Al or above ~7.3 mol Li. This concentration of Al is below what is typically reported (but not experimentally verified). The white space is the region where cubic phases exist at greater than 94 wt.%. The approximate phase boundaries are defined by the dotted lines and labeled red for the minimum Al composition necessary to achieve cubic phase stability and black for the maximum Li composition allowable for cubic phase stability.

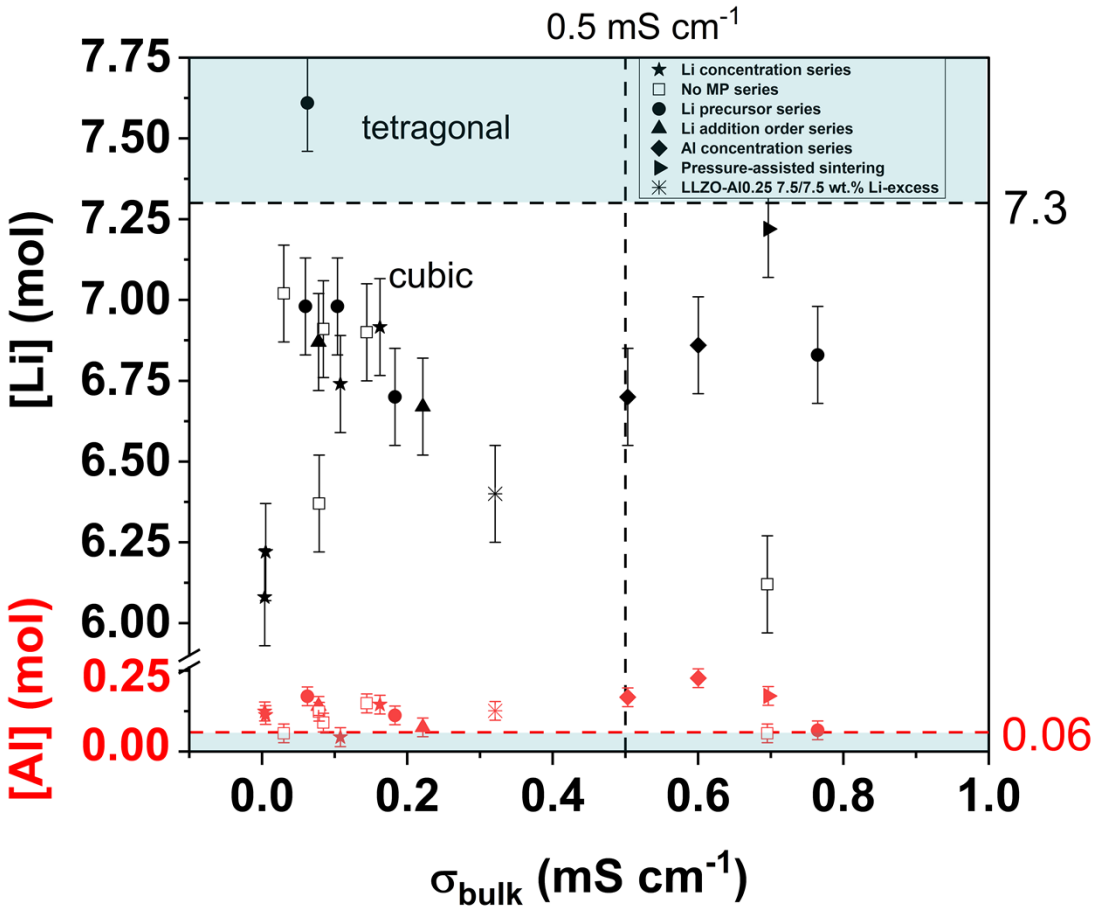

Figure 4. Al and Li concentrations (as measured by ICP) as a function of bulk conductivity and phase purity from all samples tested in this work. The red symbols are the measured Al concentrations and the black symbols are the Li concentrations. Each symbol shape corresponds to a specific series of samples as follows: Li concentration series (★), no mother powder series (□), Li precursor series (●), Li addition order series (▲), Al concentration series (◆), and pressure-assisted sintering (▶). The LLZO-Al0.25 7.5/7.5 wt.% Li excess sample (*) was part of the Li concentration series, the Li addition order series, the Al concentration series, and represents a comparable pressure-free sintering sample to the pressure-assisted sintering sample. Error bars indicate the error across all ICP measurements of the given element. Where not visible, the error

bars are smaller than the symbol. The blue regions indicate the regions of greater than 5% tetragonal phase stability. The white region denotes cubic phase stability of greater than 94% cubic stability. The red dotted line indicates the minimum concentration of Al needed for cubic phase stability. The black dotted line indicates the maximum concentration of Li allowed for cubic phase stability. The black vertical line indicates 0.5 mS cm^{-1} bulk conductivity. Individual trends are shown in the SI.

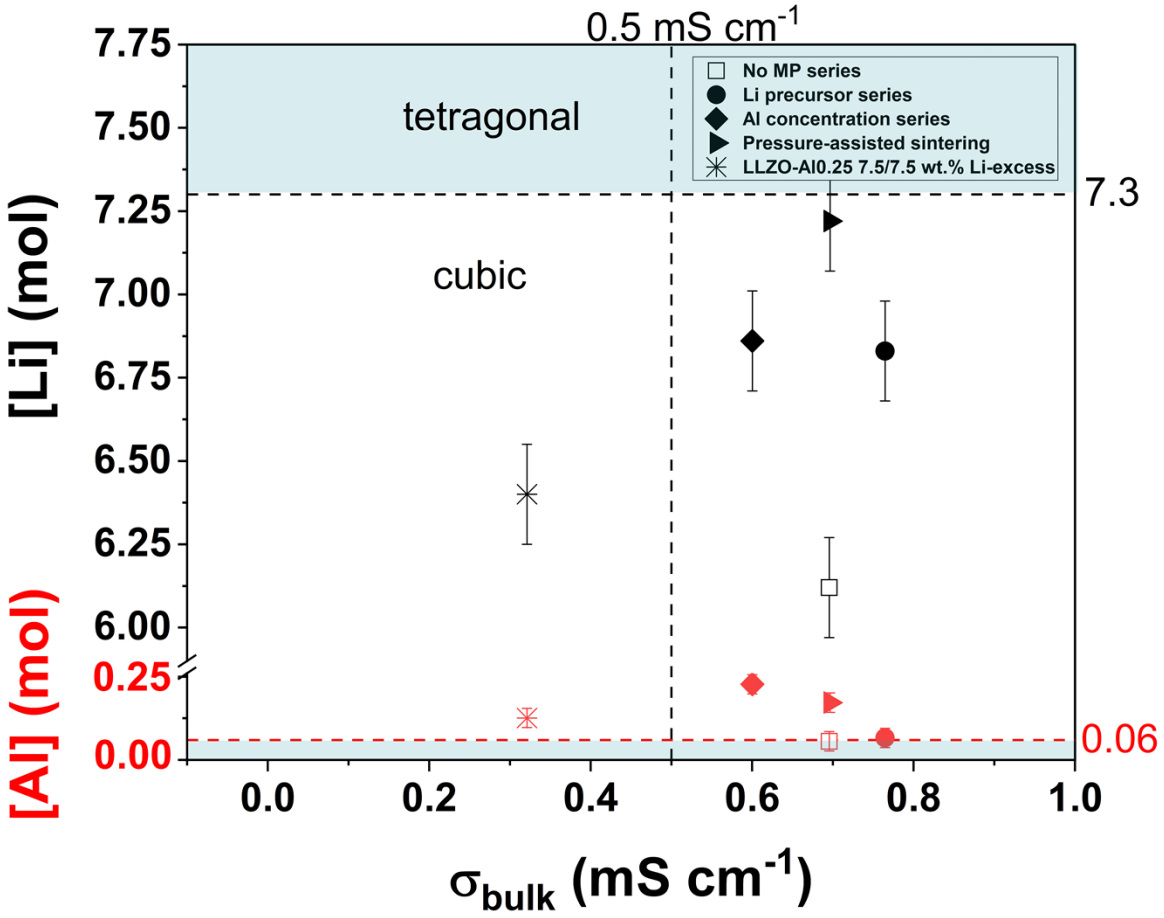

Figure 5. Al and Li concentrations (as measured by ICP) as a function of bulk conductivity and phase purity from all samples of the highest conductivities of each processing variation series. The red symbols are the Al concentrations and the black symbols are the Li concentrations. Each symbol shape corresponds to a specific series of samples. Each symbol shape corresponds to a specific series of samples as follows: No mother powder series (□), Li precursor series (●), Al concentration series (◆), and pressure-assisted sintering (▶).The LLZO-Al0.25 7.5/7.5 wt.% Li excess sample (*) was part of the Li concentration series, the Li addition order series, and the Al concentration series, and represents a comparable pressure-free sintering sample to the pressure-assisted sintering sample. It is the highest conductivity of the Li concentration series and Li addition order series. Error bars indicate the error across all ICP measurements of the given element. Where not visible, the error bars are smaller than the symbol. The blue regions indicate the regions of greater than 5% tetragonal phase stability. The white region denotes greater than 94% cubic phase stability. The red dotted line indicates the minimum concentration of Al needed for cubic phase stability. The black dotted line indicates the maximum concentration of Li allowed for cubic phase stability. The black vertical line indicates 0.5 mS cm^{-1} bulk conductivity.

When looking at the aggregate data across all conductivities, there are few clear trends for composition, phase purity, and conductivity. Indeed, there are only two samples that showed primarily tetragonal stability, with greater than 65 wt.% t-LLZO phase. These correspond to the two red stars in Figure 4 with no detectable Al concentration which is reported as 0 mol Al. These two samples had lower bulk conductivities, 0.104 mS cm^{-1} and 0.0597 mS cm^{-1}, relative to the highest reported for LLZO-Al, >0.5 mS cm^{-1}. However, the range of conductivities for the mixed phase samples of ~20-25 wt.% t-LLZO (0.03 mS cm^{-1} to 0.695 mS cm^{-1}) and the range of bulk

conductivities for the cubic samples with >94 wt.% c-LLZO (0.0039 mS cm^{-1} to 0.765 mS cm^{-1}) are wide and overlap with the conductivity values of the tetragonal samples. While majority presence of the cubic phase, and thus some amount of Al in the system, seems to allow for a higher bulk conductivity, beyond that there is little correlation between the conductivity and the phase stability. In fact, of the three samples that reach among the highest reported bulk conductivities of ~0.7 mS cm^{-1}, one is mixed phase cubic and tetragonal, and of the samples <0.5 mS cm^{-1}, most are >94% cubic phase LLZO.

From these data, it is clear that despite differences in the final Li and Al concentration, nearly all samples resulted in >94 wt.% cubic LLZO (most >98 wt.%). Beyond having the presence of at least ~0.06 mol Al in the samples, the actual concentration of Al does not have a clear correlation to bulk conductivity when looking at the aggregate of the samples from all experiments (no correlation when using the Pearson correlation coefficient and low correlation when considering the distance correlation coefficient). This lack of correlation was also observed by *Smetaczek, et al.*[53] This is exemplified by the samples with the highest reported bulk conductivity of ~0.7 mS cm^{-1}. Though all three of these samples have nearly the same conductivity, their Al concentrations range from 0.056 mol Al (~0.1 mol Al loss) to 0.172 mol Al (no detected Al loss). Some of the lack of correlation between Al concentration and bulk conductivity could be due to the fact that most of the Al concentrations measured in the samples in this study are below the Al solubility limit of ~0.35 mol, limiting the effects of secondary phases on conductivity. However, Al has been reported to play a role in reducing the conductivity within the cubic phase stability window.[23,26,28] In performing similar experiments, as shown in Figure S10, we observed an increase in the conductivity from 0.321 mS cm^{-1} to 0.600 mS cm^{-1} as the Al concentration increases from 0.126

mol to 0.227 mol, contrary to these previous works. Therefore, while it seems likely that Al does play a role in defining the conductivity of the LLZO, there may be other, more important factors, like the Li concentration, framework structure, or density, that also contribute to the observed bulk conductivity.

Like the Al concentration, the Li concentration is not correlated to bulk conductivity when considering the aggregate of results from all series (either in relation to the Pearson correlation coefficient or the distance correlation coefficient). For example, at the highest conductivities reached (~0.7 mS cm^{-1}), the Li concentration ranged from 6.12 to 7.22 mol Li. Again, this was also observed by *Smetaczek, et al.* in a microelectrode set up.[53] According to the conductivity equation ($\sigma = Ne\mu$ where N is the number of charge carriers, e is the elementary charge, and μ is the mobility of the charge carrier), the bulk conductivity should be approximately linearly correlated to the number of charge carriers, which was confirmed in previous works.[28,54,55] When looking at specific series of LLZO created through this work, there were a few instances when the Li concentration and bulk conductivity appeared correlated. In the LLZO series made with deliberate Al variation (Figure S10) the bulk conductivity increased from 0.32 mS cm^{-1} to 0.60 mS cm^{-1} as the Li increased from 6.40 mol Li to 6.86 mol Li, following the expected trend stated by the conductivity equation. However, when focusing on the Li addition order or Li excess series of LLZO, the bulk conductivity did not follow this trend with Li concentration. In the Li addition order series, the bulk conductivity decreased from 0.32 mS cm^{-1} to 0.078 mS cm^{-1} as the Li concentration increased from 6.40 mol Li to 6.87 mol Li. For the Li excess, the bulk conductivity jumped two orders of magnitude, from 0.0051 mS cm^{-1} to 0.32 mS cm^{-1} between 6.22 mol and 6.40 mol Li then dropped to ~0.13 mS cm^{-1} as the concentration increased through 6.92 mol Li,

following a similar trend as reported by *Zhang, et al.* and *Dhivya, et al.*[7,35] These contrasting correlations between Li and bulk conductivity observed between different variables repeat what was observed in the bulk conductivity relation to Al concentration, i.e. that a number of factors in processing can affect the LLZO conductivity and the controlling factor can shift according to the processing history of each sample.

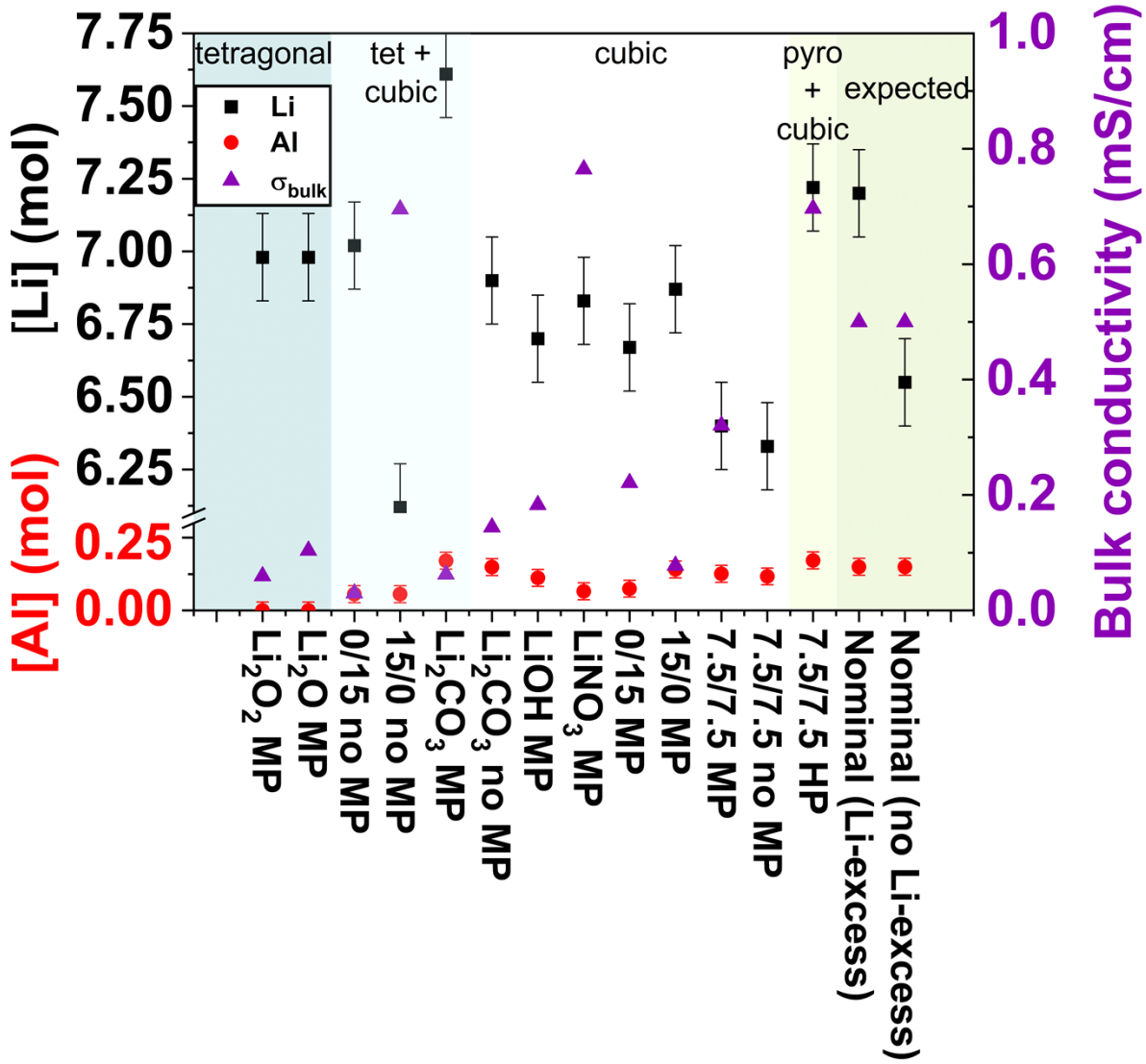

Figure 6. Composition and conductivity as a function of phase purity for all pressure-free sintered samples nominally doped with 0.15 mol Al and 15 wt.% or mol% Li excess. "MP" indicates samples sintered in mother powder. "HP" indicates the hot-pressed sample. Red circles (●) and black squares (■) correspond to the Al and Li concentration, respectively. Purple triangles (▲) correspond to the bulk conductivity. Error bars indicate the error across all ICP measurements of the given element. Where not visible, the error bars are smaller than the symbol. The dark blue rectangle region indicates the samples in that region have primarily tetragonal phase purity (>65 wt.% t-LLZO). The light blue rectangle region indicates the samples in that region have a mix of tetragonal and cubic phase stability (>5 wt.% t-LLZO and <65 wt.% t-LLZO). The white rectangle region demarcates the samples with cubic phase stability (>94 wt.% c-LLZO). The light green rectangle region demarcates the samples with a mix of cubic and $La_2Zr_2O_7$ phase purity. The dark green region includes the expected or nominal concentrations of Li and Al along with 0.5 mS cm^{-1} conductivity.

To gain a clearer understanding of the overall effects of composition on the phase purity and conductivity, Figure 6 shifts focus to the samples designed to have similar Al and Li compositions, i.e. the 0.15 mol Al samples with 15 wt.% or 15 mol% Li excess. Data can be found in Tables S1-S12. The x-axis names each of the different samples whose compositions were analyzed. The red circle above each sample corresponds to its measured Al concentration after sintering. The black square above each sample corresponds to the Li concentration measured on the sintered pellet. The purple triangle above each sample corresponds to the bulk conductivity. Phase stability regions are defined by color blocks and determined from Rietveld refinement. The dark blue region labeled "tetragonal" includes the samples that stabilized to >65 wt.% of the tetragonal phase. The light

blue region labeled “tet + cubic” encompasses the samples that stabilized to a mix of the tetragonal and cubic LLZO phases. The mixed stability range is defined by samples with >5 wt.% and <65 wt.% t-LLZO stability. The white region labeled “cubic” encompasses the samples that stabilized to >94 wt.% of the c-LLZO. The light green region labeled “pyro + cubic” highlights the sample that stabilized to the cubic phase LLZO with pyrochlore ($La_2Zr_2O_7$) as a secondary phase. The dark green region labeled “expected” shows the nominal concentration of the LLZO. Li concentrations both with and without Li excess are shown.

These samples all share a few key characteristics. First, nearly all the Al concentrations are below the nominal 0.15 mol Al, due to losses to the MgO crucible during sintering, which will be discussed below. The Al concentration shows clear trends in determining the present phases. Generally, above ~0.060 mol Al, the cubic phase is stable as the primary phase. Below 0.060 mol both the tetragonal and cubic phases are present. Once no Al is detected in the sample, the primary phase is the t-LLZO phase. This contradicts previous work in the literature that determined the transition point between t-LLZO and c-LLZO to be ~0.20 mol Al.[10,23–27] This deviation from previous literature may relate to the measured simultaneous variation in the other constituent elements of LLZO and will be discussed below. The mixed phase sample with greater than 0.060 mol Al has the highest Li concentration measured of these samples (7.61 mol Li). Thus, the Li concentration may play some role in defining the phase stability. As stated above, the elevated Li concentration of 7.61 mol may induce the ordering necessary for the t-LLZO phase to stabilize. While this sample has 5.96 wt.% t-LLZO, on average ~4 wt.% more t-LLZO than those of c-LLZO stability, the other samples of mixed phase stability in this subsection of samples have >25 wt.% t-LLZO. Therefore, it seems that the Al concentration has a more significant role in defining the

cubic stability of the LLZO structure, while the Li concentration can take a wider range while maintaining the cubic polymorph.

While Li losses are occurring, more Li remains than the nominal concentration, i.e. losses are typically less than the expected 0.65 mol Li. Nearly all sample compositions fall between the ~7.2 mol starting amount of Li (accounting for the excess) and the anticipated 6.55 mol Li that is nominally designed to be in the system. The samples where Li excess was added in two steps and were sintered with traditional sintering had compositions similar to the nominal concentration (6.55 mol Li nominal vs. 6.40 mol Li and 6.33 mol Li). Most of the rest of the samples fall in a range of 6.67 mol to 7.02 mol Li, with a few outliers above 7 mol Li and below 6.55 mol Li. A majority of the cubic samples fall in the range of 6.67 mol to 6.90 mol Li. However, cubic phase stability is observed as low as 6.33 mol Li and above 7 mol Li in this subset of samples, which falls into the cubic phase stability windows determined by *Zhang, et al.* and *Limpert, et al.*[21,35] A composition of 7 mol Li in LLZO is cited as having substantial Li ordering, leading to a transition to the tetragonal phase.[35] While the two samples that were primarily tetragonal did have compositions of ~7 (both 6.98 mol Li), other samples that were both mixed phase cubic/tetragonal and cubic were stable above 7 mol Li. Reported cubic phase stability at Li concentrations as high as and upwards of 7 mol have been previously observed.[35,56,57] While there are contrasting reports on the degree or presence of Li ordering in the cubic phase as Li concentration increases, our work combined with the previous findings of Li stability at >7 mol Li suggests that dopant induced vacancy formation of Li is not the only strategy that can be used to achieve cubic phase stability.[21,35] The lack of correlation between Li and Al concentrations observed in this work (Figures 4-6) and that of *Zhang, et al.* and *Smetaczek, et al.* supports this hypothesis.[35,53] The range

of Al and Li concentrations that are revealed through compositional analysis suggest that our understanding of the structure of LLZO and the role that vacancies and dopant play in determining the phase stability and conductivity may be different than what we had previously assumed when using the "nominal" concentrations.

As stated above, the increased Li window beyond 7 mol and beyond that required for charge balance with only Al doping paired with the lower Al concentrations than previously reported for phase stability (0.06 mol Al vs. ~0.20 mol Al) indicate that charge balancing and the structural transition from tetragonal to cubic can be controlled through other mechanisms than just the dopant concentration. If Li site vacancies are required for the transition to the cubic phase and maintaining charge balance, the vacancies must be introduced through other ways beyond Al doping. It may be the case that the vacancies are not as essential as previously believed in stabilizing the cubic phase, or it may be that the fluctuation and losses of the Zr, La, and Li during processing (as will be discussed further below) contribute to achieving charge balance and cubic phase stability. In all cases, it seems that even with cubic phase stability, the compositions of the samples can vary widely, perhaps giving insight as to the wide array of electrochemical results that have been reported in the literature and giving flexibility in the methods chosen for LLZO processing.[12,58]

4.1.3. Relationship of Lattice Constants with Phase Purity, Composition, and Bulk Conductivity

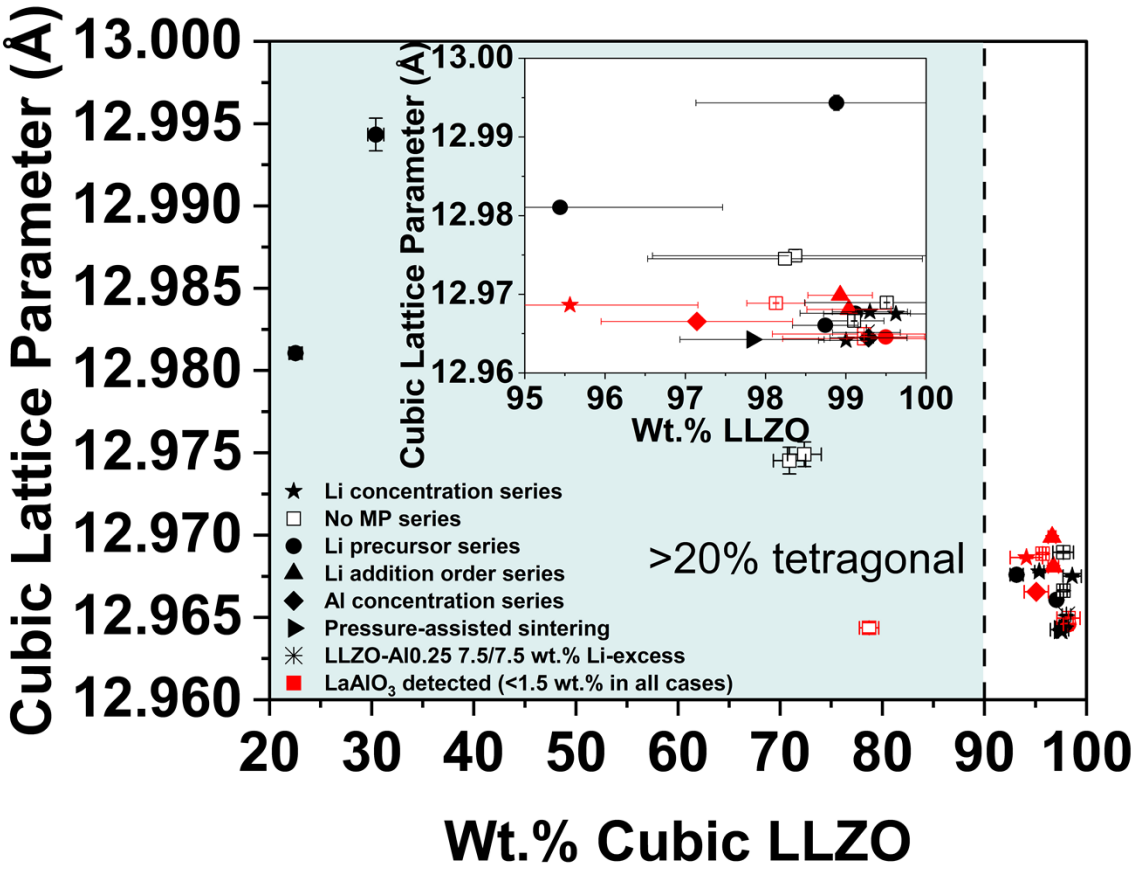

Figure 7. Cubic lattice parameter as a function of wt.% c-LLZO phase present across all samples tested in this work. Each symbol shape corresponds to a specific series of samples. Errors are reported in the SI and not included as most errors are smaller than the symbol size. Each symbol shape corresponds to a specific series of samples as follows: Li concentration series (★), no mother powder series (□), Li precursor series (●), Li addition order series (▲), Al concentration series (◆), and pressure-assisted sintering (▶). The LLZO-Al0.25 7.5/7.5 wt.% Li excess sample (*) was part of the Li concentration series, the Li addition order series, and the Al concentration series, and represents a comparable pressure-free sintering sample to the pressure-assisted sintering sample. The symbols of the samples where $LaAlO_3$ is detected from XRD are colored

red. Where error bars are not visible for the lattice parameters or phase percentage, they are smaller than the symbol.

There are a few clear trends across the cubic lattice parameter and the LLZO phase stability. This can be observed in Figure 7 and Tables S2, S4, S6, S8, S10, and S12. First, all studied samples are >95 wt.% LLZO, showing overall exceptional phase purity. Only 5 samples are <90 wt.% c-LLZO or >20 wt.% t-LLZO, again displaying remarkably high c-LLZO phase stability across all processing and synthesis parameters tested as well as resulting compositions, suggesting, again, the favorability of the cubic phase. Second, nearly all samples are clustered in the same cubic lattice parameter window of 0.01 Å between 12.964 Å to 12.974 Å. These values align well with previous literature.[9,17,26,28,58] Therefore all samples of >94 wt.% cubic LLZO can be considered to have similar lattice parameters, despite the variation in processing. The only samples that lie significantly outside of the 12.964-12.974 Å range are the two samples with >65 wt.% t-LLZO stability with lattice parameters of 12.98 Å and 12.99 Å. While this increased c-LLZO lattice parameter may indicate a transitional cubic state between the c-LLZO and the t-LLZO, the heightened lattice parameter may be an artifact of the heavily overlapping peaks of the t-LLZO and the c-LLZO (Figure S13), which would have a greater effect in the majority t-LLZO samples. This phenomenon of invariant lattice parameters extends to the lattice constant as a function of the Li and Al composition (Figures S14, S15). In both cases, the lattice parameter does not change as a function of either the Li or Al concentration. This aligns well with some previous work,[28,34] but contradicts work by *Parascos, et al.* that claims a decrease in lattice parameter with an increase in Al concentration, though the overall decrease is less than 0.01 Å.[26] The constant lattice parameters as a function of the processing variation and composition found in this work paired with minimal

changes in previous literature suggest that these variables have little effect on the overall structure of the LLZO, perhaps due to the fact that the Al is substituting into an interstitial site rather than a framework structure site. Therefore, any changes in composition are likely limited to a change in occupancies or local distortions in the lattice, which will be discussed further below.

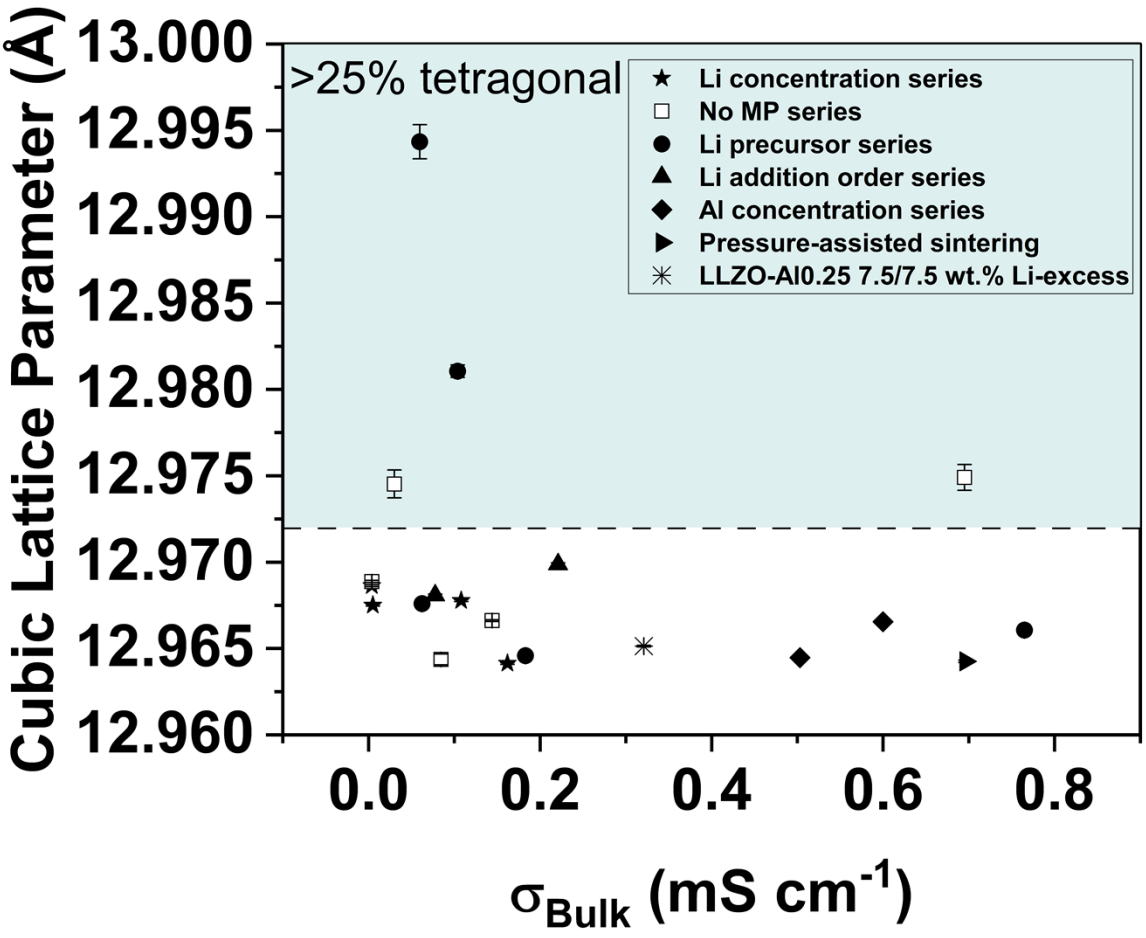

Figure 8. Cubic lattice parameter as a function of bulk conductivity across all samples tested in this work. Each symbol shape corresponds to a specific series of samples as follows: Li concentration series (★), no mother powder series (□), Li precursor series (●), Li addition order series (▲), Al concentration series (◆), and pressure-assisted sintering (▶). The LLZO-Al0.25

7.5/7.5 wt.% Li excess sample (*) was part of the Li concentration series, the Li addition order series, the Al concentration series, and represents a comparable pressure-free sintering sample to the pressure-assisted sintering sample. Where error bars are not visible for the lattice parameters, they are smaller than the symbol. The blue region is the region in which samples are >25 wt.% t-LLZO. The white region includes samples with cubic phase stability of greater than 90% c-LLZO.

Figure 8 is the cubic lattice parameter determined by Rietveld refinement as a function of the bulk conductivity for each sample synthesized in this study. Values for both the lattice parameter and the bulk conductivity are also shown in Tables S1-S12. As with the phase purity and compositions, the lattice parameters are independent of the bulk conductivity. This aligns well with previous experimental reports on Al-doped LLZO and computational reports on LLZO doped on the La and Zr site.[27,59] Since the lattice parameter is defined by the overall framework structure,[60,61] this suggests that structural framework is not a predictor of the bulk conductivity and that changes in the structure that affect the conductivity are likely related to shifts in the local structure or occupancies. These shifts will be discussed further below.

4.2. Li, Al, La, and Zr Losses in LLZO Processing

Through extensive experimental studies the results demonstrate significant mass transfer of Li, Al, La, and Zr during high temperature synthesis. As a general trend, there are decreases in Li and Al concentrations, especially during the sintering phase while decreases in Zr and La are present largely during calcination (Figure 9; Figures S1, S3, S6, S8, S10, S12; Tables S1-S6). The Li and Al losses can both generally be observed through a decrease in the final composition as compared to the intended starting compositions. However, the Zr losses are observed through the increase in

Li and Al concentrations during calcination of each sample as illustrated by the black arrows in Figure 9. Figure 9 shows this trend in the Li excess series, though it is generally observed across all processing series (Figures S1, S3, S6, S8, S10, S12). The reported Li and Al concentrations per formula unit (y-axes of Figure 9a and b) are calculated by normalizing the ICP concentration of each element by the ICP concentration of Zr. Since gains in Li and Al are not likely, the increase in their concentrations during calcination can be attributed to Zr losses. Likewise, the constant La concentrations during calcination suggest a relative loss of La during calcination. These combined elemental losses result in significant variation in composition compared to nominal starting values, but still result in cubic LLZO with high ionic conductivity. These losses are likely occurring to the MgO calcination/sintering crucible and are likely facilitated by concentration gradients, Li or Li-rich secondary phases, and intermediary reaction phases, such as $La_2Zr_2O_7$ and Li_2ZrO_3.

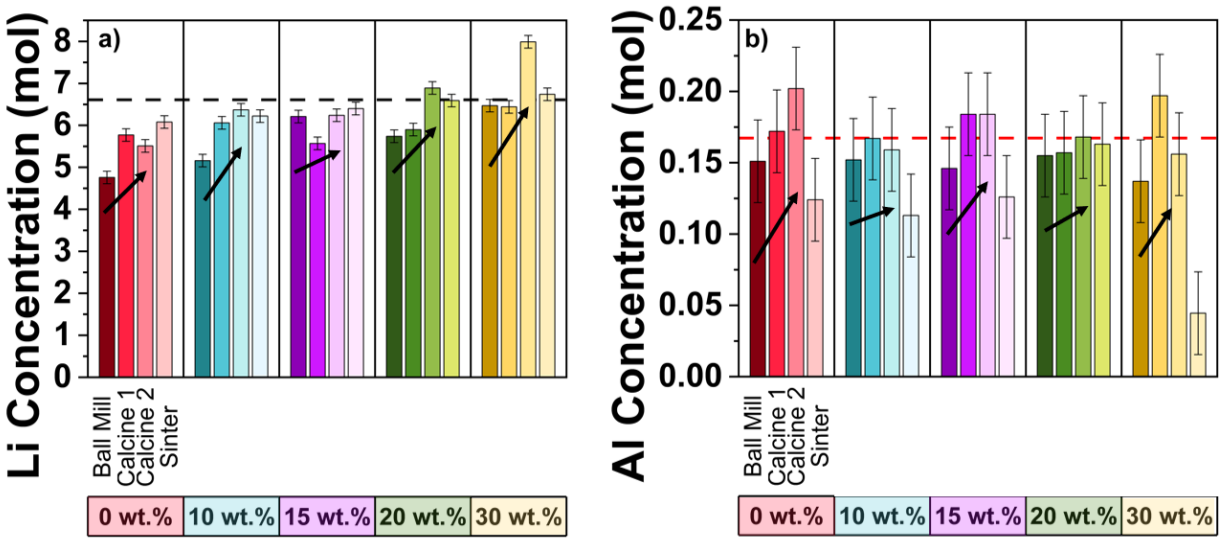

Figure 9. a) Li concentration and b) Al concentration in mol as a function of processing step and Li excess concentration. Red boxes correspond to 0 wt.% Li excess, blue boxes to 10 wt.% Li excess, purple boxes to 15 wt.% Li excess, green boxes to 20 wt.% Li excess, and yellow boxes to 30 wt.% Li excess. The processing step from ball milling to sintering progresses from darkest to

lightest color in each sample. Dashed lines indicate the nominal Li and Al concentrations. Arrows show the increase in Li and Al concentrations through calcination.

4.2.1. Li Losses

The 0-30 wt.% Li excess series captures many of the Li loss phenomena that were observed across the multiple series in this work and will be examined here to explain the origin of potential Li losses during processing. Contrary to findings by *Limpert, et al.* and *Liu, et al.* and in line with findings by *Schwab, et al.*, the amount of Li lost from the nominal excess amount increases as the amount of Li excess increases, as shown in Figure S4.[21,33] For example, in the 0 wt.% Li excess, ~0.17 mol Li is lost from the nominal excess (comparable to the ICP detection limit of ~0.15 mol Li) while for 30 wt.% Li excess, ~1.52 mol of Li is lost from the expected nominal Li concentration including the excess. The main difference between this work and those of *Limpert, et al.* and *Liu, et al.* is the dopant.[21,33] While Al was the dopant used here, *Limpert, et al.* and *Liu, et al.* used Nb and Ca co-doping and Ta-doping, respectively. Since the Li and Al precursors would be intermixed throughout the pellets, there may be an increased formation of Li-rich liquid phases that would be proportional to the amount of Li excess in the system throughout the pellet, which is what is roughly observed in Figure S4. Meanwhile in the samples where Al is only diffusing in from the crucible, as is the case for *Liu, et al. and Limpert, et al.*, these Li-rich liquid phases associated with the Li_2O-Al_2O_3 eutectic phase may be largely reacted into the LLZO by the time the Al diffuses throughout the pellet, decreasing the effect of Li loss as a function of Li excess.[62] Similar to the Al, the Ga substitute is also hypothesized to act as a sintering aid, likely leading to the similar results observed between LLZO-Al and LLZO-Ga.[34] Overall, this difference in Li loss highlights the importance of the effect of doping element on the final properties of the LLZO. While there

was still an overall increase in the Li concentration corresponding to the increase in Li excess, the amount of Li excess added to a sample to obtain the desired Li concentrations will depend on the dopant, i.e. Al, Nb, Ta, Ga, etc.

Interestingly, when observing samples that were sintered with and without mother powder (Figure S8, Table S7), the mother powder does not seem to play a consistent role in preventing Li loss. Only the samples where all Li excess was added before ball milling had higher Li concentrations when mother powder was used compared to samples sintered without mother powder (7.61 mol vs. 6.90 mol Li and 7.27 mol vs. 6.12 mol for Li_2CO_3 15 mol% Li-excess and 15/0 Li addition, respectively). In these samples, those sintered in mother powder had higher Li compositions than the calcined powder, suggesting that the Li in the mother powder may diffuse to the sintering LLZO, though it is not entirely clear why there would be a driving force for Li to preferentially diffuse to the sample as the Li concentrations should be the same. The effect of comparable increase in Zr loss, as will be discussed below, may impact the observed Li concentrations after calcination. For the samples where the Li excess was added in two steps or where Li excess was only added between calcinations the samples with and without mother powder had similar Li concentrations: their values were within or very close to the error of ±0.15 mol. This finding suggests that adding Li between calcination steps can prevent Li loss and negate the need for mother powder, at least in relation to Li composition. While the mechanism is not entirely clear, it may be that the Li is volatile or more stable in the LLZO when Li excess is added at a later stage and that the precursor phase may decrease the driving force for Li migration from the mother powder to the samples or increase the loss of Zr from the LLZO. Regardless, it appears that effectiveness of mother powder in preventing Li loss is not consistent and may be dependent on

the timing of the Li addition, suggesting that multiple processing parameters are affecting the final Li concentration beyond the explicit addition of Li or presence of Li mother powder.

4.2.2. Al Losses

Another common observation throughout the series tested above was the decrease in Al concentration during sintering. This was particularly noticeable in the loss of all previously detectable Al in the LLZO samples made from Li_2O_2 and Li_2O, with 0.079 mol and 0.149 mol Al lost, respectively. In previous works on LLZO, either undoped or synthesized with other dopants, Al was often observed in the final, sintered product.[13,17,21,33,34] The appearance of Al in the samples has been attributed to the diffusion Al from the Al_2O_3 calcination and sintering crucibles.[17] Several groups noted that an increase in the Li excess correlated to an increase in the amount of Al diffused into the LLZO.[13,21,33] *Limpert, et al.* observed an increase from 0 mol Al to 0.550 mol Al for samples ranging from 0 wt.% Li excess to 20 wt.% Li excess.[21] In the case where there was no change in Al concentration with increasing Li excess, the substitute shared the same site as the Al, suggesting that the amount of Al uptake was limited by co-occupation of the sites.[34] *Liu, et al.* determined that the increase in Al uptake originated from an interaction between the Li salts and the Al_2O_3.[33] This aligns with the observation of $Li_{0.5}La_2Al_{0.5}O_4$ at the grain boundaries of LLZO-Ta sintered in Al_2O_3 by *Li, et al.* as well as the Li_2O-Al_2O_3 phase diagram produced by *Cook, et al.* that shows liquid phase formation between the two at temperatures as low as 1055 °C.[13,62] In all above cases where undoped LLZO uptakes Al from the Al_2O_3 crucible, there is a clear potential chemical gradient of Al between the LLZO and the Al_2O_3, creating a driving force for Al to diffuse into the LLZO.

In our case, the potential gradient is flipped. Here, the Al concentration is in the LLZO-Al and an Al sink is present in the form of the MgO crucible. Al_2O_3 is only able to form a solid solution up to 0.01% with MgO at temperatures close to where we are sintering (1300 °C vs. 1225 °C).[63] While this does not seem significant, the total amount of Al, considering the 0.5 g size of the individual pellets, the <0.1 mol Al lost per sample, and the comparatively large size of the MgO crucible relative to the pellets, 0.01% solubility could be sufficient to lead to the observed Al losses in the LLZO.

It may be, as hypothesized by *Liu, et al.*, that the Li salts facilitate the diffusion of Al.[33] In our case, the heightened Li concentrations of 15.60 mol Li and 9.51 mol Li in the twice calcined powders of Li_2O_2 and Li_2O, respectively, was correlated to the loss of all Al from the samples while Li concentrations of <7 mol Li in the Li_2CO_3 and LiOH did not lead to any observed Al loss. Meanwhile, $LiNO_3$, with a Li concentration between the two at 7.64 mol Li after the second calcination, had ~50% Al losses. Across all samples and series, increases in Li concentration in the calcined LLZO powders (>~7 mol) led to larger decreases in the Al concentration on sintering (i.e. Figure S4 and Figure S6) as compared to calcined samples with <7 mol Li. As mentioned above, a similar observation was made by *Liu, et al.*, *Limpert, et al.*, and *Li, et al,* but with an increase in Al concentration in the LLZO with an increase in Li concentration.[13,21,33] Interestingly, similar results were obtained by *Schwab, et al.* with LLZO-Ga: they observed Ga loss after sintering for more than 10 hours in an Al_2O_3 crucible in samples with greater than 10% Li excess, suggesting a similar loss mechanism for both substitutes.[34] These works, combined with our own observations, suggest that Li (in the LLZO, in the precursors, or in intermediary phases) plays a role in facilitating diffusion of Al.

Additionally, the loss of Al is very highly linearly correlated to the Al composition of the LLZO after the second calcination. In Figure S10, the Al concentration increasingly drops by more significant amounts, 0.058 mol, 0.085 mol, to 0.164 mol, as the Al concentration in the calcined powder goes from 0.184 mol, 0.263 mol, to 0.391 mol Al. This may be due to the higher concentration gradient of the Al between the LLZO-Al and the MgO crucible, which would be predicted to contribute to the greater comparative losses by Fick's First Law of Diffusion.

The Al loss in the system is consistently ~0.035 mol Al greater or 1.6 times as much without the presence of mother powder as compared to the same samples sintered with mother powder. Based on the hypothesis that the loss of Al is due to the concentration gradient between LLZO-Al and MgO, this suggests that a mother powder bed between the crucible and pellet can act as a buffer layer for this diffusion. The Al will first diffuse from the mother powder, initially protecting the pellet from Al loss. However, over time (30 hours) at high temperatures (1225 °C), the mother powder will lose enough Al that there will be a concentration gradient at the pellet interface, leading to some losses of Al to the MgO through the depleted mother powder. The difference in Al in the sintered pellet with and without mother powder provides another piece of evidence to suggest that the Al is lost through the interface with the MgO.

There appear to be minimal Al losses when densification is pursued through hot-pressing in a graphite die (Figure S12, Table S11). The lack of Al losses may be due to the change in the material directly contacting the LLZO. Carbon is not known to uptake Al, potentially minimizing Al losses and emphasizing the importance of material selection when considering sample contact during

sintering. Additionally, the decreased sintering time of 40 minutes vs 30 hours could play a role in decreasing the Al losses. In summary, not only the choice of surrounding material of the sintering/densifying pellet is important, but also the process in which the samples are sintered could affect the Al losses in the system.

4.2.3. Zr and La Losses

In many of the above LLZO series, an increase in the Li and Al is observed through the calcination steps. This is clearly illustrated in the Li excess series of LLZO samples. Al is not likely to be increasing in the sample as there is no external source to provide Al. While some Li increases may be expected at the addition of excess Li between the two calcination steps, the observed increases are greater than expected. For example, in the 0/15 Li excess sample of the Li addition variation series, the total Li addition is 0.4 mol lower than what is measured after the second calcination (Figure S6). As Li is not being added to the LLZO sample to concentrations greater than expected values, there must be another reason for the increase. The molar concentration of the Li and Al in the samples are determined by normalizing by the ICP detected Zr concentration. If the Li and Al are not increasing, the Zr concentration must be decreasing during these steps, leading to the rise in the observed Li and Al concentrations. While the Li and Al phases increase in concentration, the La concentration remains constant. Since it is likely that the concentration of Zr is decreasing as the processing proceeds, the constant La concentration indicates La losses may simultaneously be occurring. Interestingly, *Schwab, et al.*, when normalizing to the La concentration, observed a decreased Zr concentration after the first calcination paired with a constant La concentration in LLZO-Ga, though origins of the losses were not known and other measured elements (Li, Ga) did not see the same increases as observed in this work.[34] In this work, the finalization into the cubic phase and return of Li and Al concentrations

to approximately what is expected (if anything, lower than expected for Al), indicates that the Li and Al losses "catch up" with the Zr and La losses, and stabilize into the expected LLZO cubic phase.

The loss of Zr may have similar origins as the loss of Al. In cases where the Li excess is larger, there appears to be a larger increase in the Li concentration, indicating a larger decrease in Zr concentration. For example, in the 0/15 sample of the Li addition variation series, after the first calcination, there are no observed Li losses (Figure S6). However, once 15 wt.% Li excess is added, the Li composition after the second calcination is ~1.4 mol vs. the added ~1 mol of Li. Likewise, in the 15/0 sample of the same series, the Li concentration jumped ~0.6 mol between ball milling and the first calcination, when only Li losses are expected. However, after the second calcination, there was no change in the Li concentration. The Zr losses appear to be correlated to Li excess and happening largely during the calcination steps, suggesting that Zr is lost during the reaction of the precursors or the intermediary phases into LLZO and facilitated by Li concentration. It is known that the Li_2ZrO_3 phase is formed as an intermediary to LLZO and is in a melt state at the calcination temperature.[64] It may be that this phase, or other similar Li- and Zr-rich phases, are playing a role in the Zr loss.

Since it is highly unlikely that a Zr phase should be subliming, it appears that the MgO crucible may again be playing a role in the elemental loss. Looking at the MgO-ZrO_2 phase diagram, Zr- and Mg-based phases can form solid solutions at temperatures slightly higher than what is reached here (>1240 °C). In addition to the possibility that the Zr is lost to the MgO directly, it may also be that the Zr-rich liquid phase is left behind in surface crevices of the MgO crucible after

calcining. Since the losses of the La are proportional to those of the Zr, they may be lost through similar mechanisms or pathways. Though a ternary diagram of La-Mg-O is not known, the similar ratios of the elemental distribution between the $La_2Zr_2O_7$ pyrochlore phase suggests this phase may be involved in facilitating Zr and La losses. In fact, in samples with pyrochlore present, such as the 0 wt.% Li excess sample and the sample nominally doped with 0.25 mol Al, perceived Li concentrations increase without mother powder where in most other samples there is no perceived change in Li concentration with or without the mother powder (Figure S8, Table S8, Figure S9). This suggests that the $La_2Zr_2O_7$ preferentially facilitates Zr and La losses to the MgO crucible and that the mother powder can play a role in buffering these losses. Therefore, it may be that there are several factors that can lead to the Zr loss during sintering, including those associated with losses of other elements, such as La.

Figure 10 is a schematic of the elemental losses that are occurring through processing, as observed by the ICP measurements. The white "synthesis step" region in the middle mirrors Figure 1a and shows the processing steps in synthesizing LLZO. The "losses" section is in yellow below the processing steps. The box is below the step at which these elements, in bold in the box, appear to largely be lost, i.e. Zr, La, and Li are potentially lost in the calcination phases while Li and Al are largely lost in the sintering stage. Potential phases that either facilitate or lead to the loss are featured below the bolded elements and where the elements are physically lost to are in the white boxes below. The blue boxes show the evolving elemental composition of the LLZO after each processing step. We assume we are starting with nominal $Li_{6.55}Al_{0.15}Zr_2La_3O_{12}$. The stoichiometry of a given element is subtracted from when losses occur in preceding step, as defined by the yellow boxes. In the end, the cubic, Al-doped LLZO stabilizes due to the accumulation of elemental losses

throughout the procedure, albeit into cubic LLZO samples with a wide range of Li, Al, Zr, and La compositions.

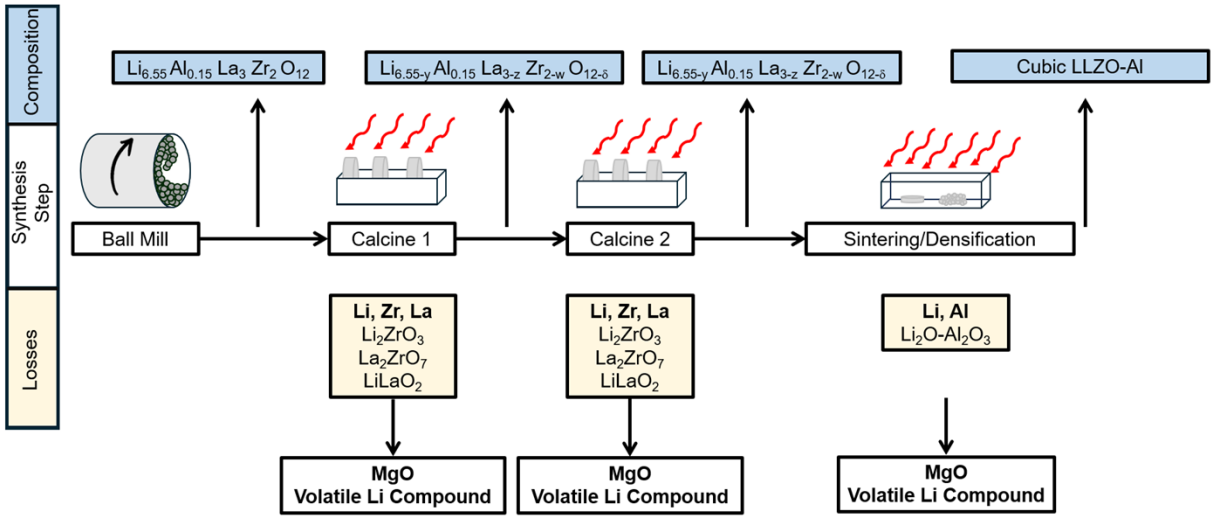

Figure 10. Schematic showing the processing steps of Al doped LLZO in middle white squares, the lost elements and their potential associated phases are in yellow on the bottom half of the schematic, and the losses by element in the top half of the schematic as measured at the end of each processing step. The bottom row of boxes indicates where the elements are lost to. Enough relative losses occur throughout the process in each element that cubic LLZO is generally stabilized.

4.2.4. Effect of Crucible on Composition of LLZO

As further evidence to support the hypothesis that the lost elements (Li, Al, Zr, La) in the LLZO go to the MgO crucible, a clear discoloration of the crucible is observed where LLZO has contacted the MgO. Figure 11 shows three angles of a magnesia crucible used for calcination and sintering of only LLZO for this work. The outside of the crucible is shown in Figure 11b and cross sections of the crucible are shown in Figure 11a and c. The “LLZO contact” label is written approximately

where the LLZO samples touched the crucible, either during calcination or sintering. The purple arrow indicates the discoloration of the sample from calcination from an off-white to a peach color. Figure 11a is the cross-section of the side and bottom of the crucible. The peach color is both where the samples contacted (the bottom of the crucible) as well as further down into the bottom and sides of the crucible. Figure 11b is the outside of the crucible. In calcination, the ~25 mm pellets rest on the upper edge of the crucible wall. A peach semi-circle shape can be seen from the edge of the wall, extending radially from the contact point. Figure 11c is a cross-section of the bottom of the crucible where the sintered pellets sit. The peach color splits the cross-section in half. In all cases, it seems that wherever there is contact with the LLZO during sintering or calcining, there is a discoloration of the MgO crucible, further suggesting an effect of the LLZO on the crucible. Since there is no other clear compositional or structural change in the LLZO beyond the elemental losses, it seems likely that the change in the MgO is due to the diffusion of the elements lost from the LLZO structure into its own surface and structure. The continued diffusion beyond the surface suggests that the MgO acts as a sink for some or all of the lost elements (Al/Zr/Li/La) to diffuse from the LLZO and that the impurities readily diffuse through the material.

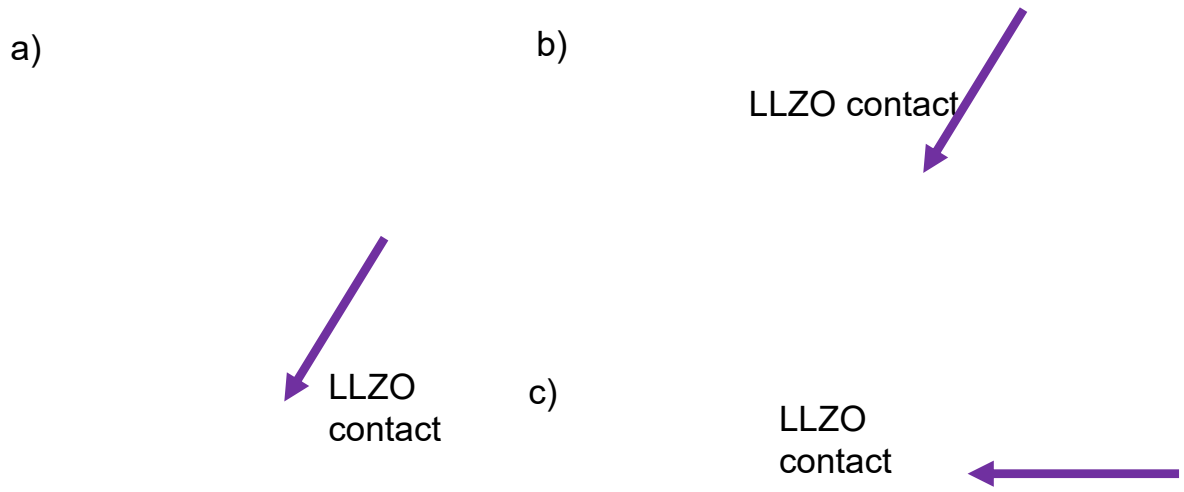

Figure 11. Magnesia crucible used for calcining and sintering pellets. a) Cross-section of the crucible with one of the walls and bottom of the crucible shown. b) Outside of the crucible. c) Cross-section of the bottom of the crucible. The "LLZO contact" label indicates the surface where the LLZO was in contact with the crucible. The purple arrow indicates the peach color that appears where the LLZO made contact and where the color spread.

To further check the hypothesis that these elements are diffusing into the MgO, the XRD of the crucible, both in the white and peach sections was performed and is shown in Figure S16. In both cases, the diffraction peaks are primarily those of MgO (space group *Fm-3m*). While the secondary phases are difficult to identify due to their low peak intensities, there are clear differences in the relative peak intensities of the magnesia itself. For example, the peak height intensity ratio between $2\theta = 42^{o}$ and $2\theta = 62^{o}$ shifts from 2.7 to 2.0 when comparing the white MgO to the peach MgO. Relative intensities are related to the occupancy and static and dynamic disorder of the atoms in that particular plane. Therefore, this shift in the peak intensities suggests a change in the atomic occupancies of the structure. Due to the presence of Mg sites in all of the planes contributing to

these two peaks ((200), (020), (002) for the peak at 2θ = 42° and (2-20), (20-2), (02-2), (220), (202), (022) for the peak at 2θ = 62°), this change in relative intensity could potentially be due to the substitution of Al, Li, La, or Zr for Mg. In addition to the change in color and XRD peak intensity variation, preliminary XPS data shows that the peach-colored areas of the MgO, again the areas that have been in contact with LLZO, have increased intensities of Zr compared to the white, untouched areas of the MgO. This further supports the notion that the Zr is leaving the LLZO or its precursors and going towards the MgO. Since XPS is specifically a surface sensitive technique, these results suggest that the Zr, in addition to potentially entering the MgO, is leaving the LLZO and enriching the MgO surface or remaining stuck to the surface in the form of Zr-rich secondary phase, such as Li_2ZrO_3 or $La_2Zr_2O_7$.

Regardless, the discoloration of the MgO crucible and simultaneous decrease in Li, Al, Zr, and La (as observed through the increased Li and Al concentrations prior to sintering) suggests that the MgO crucible, though initially used to replace Al_2O_3 crucibles that doped LLZO with Al, is also playing a role in defining the composition of the LLZO by providing a sink for Al, Zr, La, and Li loss. This is especially important as the loss of Al can play a role in controlling the conductivity of the cubic LLZO, both through its site blocking and defect trapping, as well as through the phase transition from the low conductivity tetragonal phase to the high conductivity cubic phase, as discussed above.[27,65–68] Similarly, the presence of Li vacancies is theoretically what leads to the transition from the tetragonal phase to the cubic phase as well as controlling the number of charge carriers, both of which contribute to defining the bulk conductivity.[18] Meanwhile, the losses of La and Zr provide for an unexpected flux in the charge balance and structure of the LLZO, supporting the hypothesis that compositional control of the cubic phase may go beyond that of the

dopants. Additionally, as discussed below, this flux may directly affect the conductivity by altering the framework structure. Interestingly, the losses of Li, Ga, and Zr reported by *Schwab, et al.* in LLZO-Ga processed in Al_2O_3 crucibles suggests that other crucible materials may also be acting as sinks to LLZO elements.

As discussed above, it seems that Li, either as a precursor, intermediary phase, or in LLZO, may be playing a role in facilitating the observed Al losses in the LLZO. This is further supported by the lack of color change observed at the contact points between the Al_2O_3 tube used in the tube furnace and the MgO crucible. This lack of color change suggests a fundamental difference between the Al_2O_3 and the LLZO-Al and its precursors that is leading to this interfacial interaction with the MgO. It may be that the comparative thermodynamic stability of the Al in the Al_2O_3 vs. the LLZO-Al is higher, leading to a lower likelihood for the Al to leave the Al_2O_3 for the MgO.

4.3. Overall Effects of Processing and Composition on Density

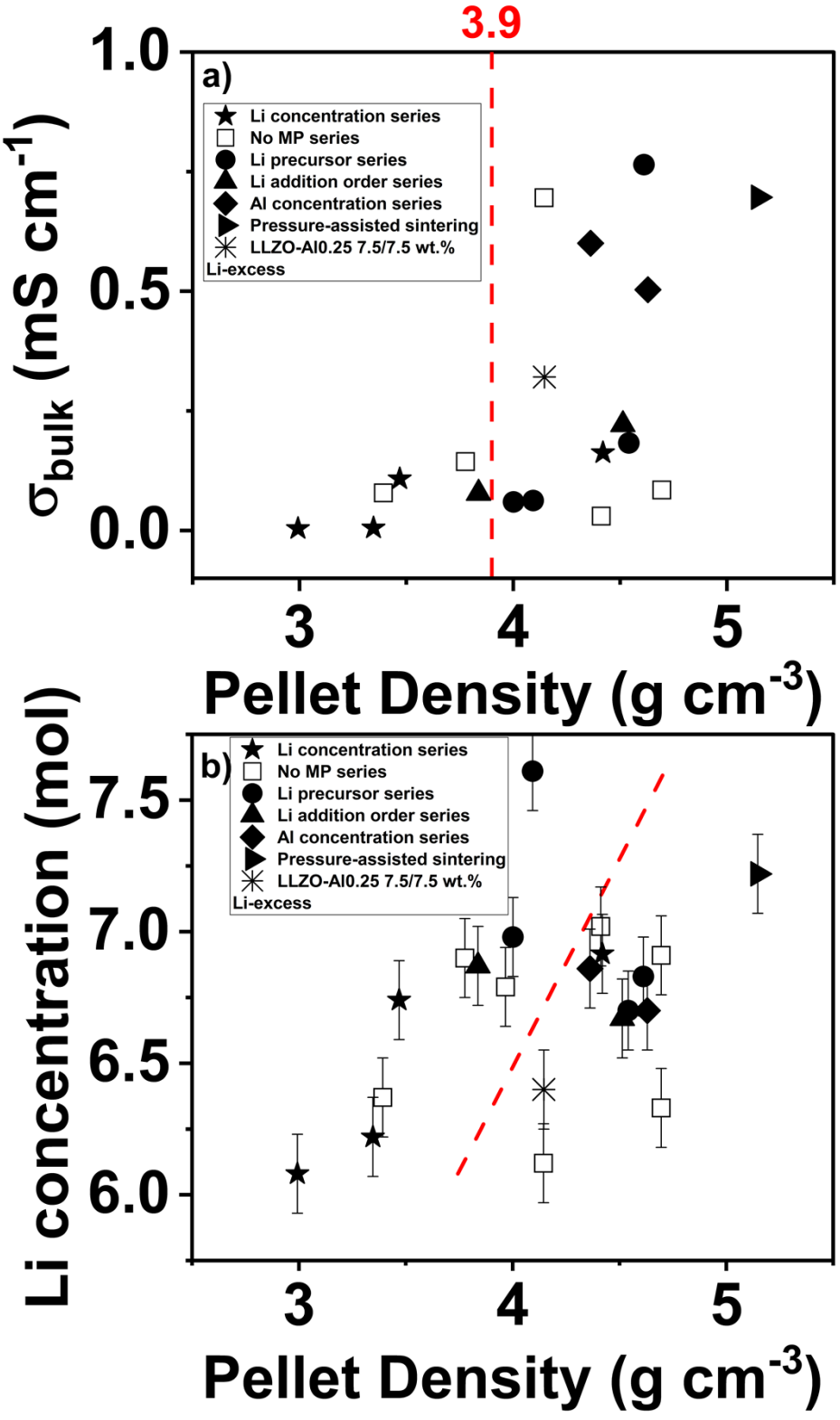
3.9
a)
Li concentration series
No MP series
Li precursor series
Li addition order series
Al concentration series
Pressure-assisted sintering
LLZO-Al0.25 7.5/7.5 wt.%
Li-excess
σbulk (mS cm-1)
1.0
0.5
0.0
3
4
5
Pellet Density (g cm-3)
b)
Li concentration series
No MP series
Li precursor series
Li addition order series
Al concentration series
Pressure-assisted sintering
LLZO-Al0.25 7.5/7.5 wt.%
Li-excess
Li concentration (mol)
7.5
7.0
6.5
6.0
3
4
5
Pellet Density (g cm-3)

Figure 12. Density of all samples tested as a function of a) bulk conductivity and b) Li concentration. Each symbol shape corresponds to a specific series of samples as follows: Li concentration series (★), no mother powder series (□), Li precursor series (●), Li addition order series (▲), Al concentration series (◆), and pressure-assisted sintering (▶). The LLZO-Al0.25 7.5/7.5 wt.% Li excess sample (*) was part of the Li concentration series, the Li addition order series, the Al concentration series, and represents a comparable pressure-free sintering sample to the pressure-assisted sintering sample.

Figure 12 is an accumulation of density data taken from each of the samples across the different LLZO-Al series described above. There are a few key trends that appear once the results from all samples are accumulated. Figure 12a is the bulk conductivity as a function of density. The dotted line at 3.9 g cm^{-3} (~75% relative density) indicates the minimum density necessary to achieve heightened conductivity levels. Below, bulk conductivity levels are restricted to <0.15 mS cm^{-1}. Above this line, the bulk conductivity can range as high as 0.76 mS cm^{-1}, which is among the highest conductivities reported for LLZO-Al.[1,36,40] In previous works on LLZO, an increase in conductivity as the density increased was also observed, with minimum densities for high conductivity ranging between ~83% relative density and ~95% relative density.[13,33,69] It is important to note that in these reports, they could not distinguish the grain from the grain boundary, so they reported the total conductivity, meaning that the grain boundary character could play a role in their results where they are not directly accounted for in ours. Regardless, similar patterns arise between our samples and previous works. *Liu, et al.* and *Huang, et al.* also observed a step-wise increase in conductivity, in some cases as much as 2 orders of magnitude, after a minimum density threshold was achieved.[33,69] In both of those works, the conductivity remained roughly constant

after the minimum relative densities of 83% and 95% were reached. While our minimum threshold for heightened conductivity is lower, potentially due to the contribution of the grain boundaries to their reported conductivities or due to variation in processing parameters between our studies and theirs, it seems that there is a maximum amount of tortuosity in the sample that can be tolerated before the bulk conductivity is affected. In the case of our data set, that maximum level of tortuosity corresponds to 3.9 g cm^{-3} or ~75% relative density of the pellet. Above that, the limiting factor for bulk conductivity is no longer the density and other factors, such as the composition, phase purity, and processing, play a more prominent role in defining the conductivity. As all of these samples had a variety of processing histories, their conductivities varied once density was no longer the controlling factor. In comparison, all the above-cited studies focused only on one or two processing variables, leading to a plateau after the minimum tortuosity was overcome for high conductivity. These results indicate that to maximize the bulk conductivity, only a minimum of 3.9 g cm^{-3} is needed, and from there, other aspects that control the conductivity can become the focus of conductivity optimization. Interestingly, the threshold of 75% relative density for maximized Li conduction aligns well with previous work performed on the sulfide solid electrolyte, Li_6PS_5Cl.[70] In their case, a plateau in total conductivity occurs at 75% relative density after the grain boundaries no longer have a detectable effect on the conductivity.[70] The similar results in maximum tortuosity for maximizing bulk conductivity suggests that this minimum relative density is more generally applicable across the different solid electrolyte classes.

Figure 12b shows the pellet densities as a function of Li composition. The dashed lines correspond to the best fit line of the data and are added to highlight the observed trends. There is a low correlation (based both on Pearson's and distance correlation coefficients) between the Li

concentration and the density. Though not strong, this low correlation between Li concentration or Li excess and density has been previously observed by several groups,[13,30,33,69] though *Huang, et al.* observed a plateau at ~95% relative density after a minimum Li concentration was reached and *Schwab, et al.* observed a peak in higher relative densities of ~94% with 5% Li excess.[30,34] In this work, an increase from 2.99 g cm^{-3} to 4.42 g cm^{-3} was observed in the range from 0 wt.% Li excess to 20 wt.% Li excess with a decrease to 3.47 g cm^{-3} at 30 wt.% Li excess. With respect to the density, the Li precursor and its related melt plays a role as a sintering aid.[21] Further, the loss of material to the crucible may play a role in the reaction mechanism and resulting densification. Therefore, the increase in Li precursor leads to both an increase in the final Li that is present, as can be observed in Figure S4, and an increase in the amount of melt phase that is likely to have formed and assisted in the densification of the pellet. Table S1 also highlights the density as a function of the Li precursor. The density for the Li_2CO_3, LiOH, and $LiNO_3$ are 4.09 g cm^{-3}, 4.54 g cm^{-3}, and 4.61 g cm^{-3}, respectively. The increased density increases as a function of the melting temperature of each of these precursors. Li_2CO_3, LiOH, and $LiNO_3$ have melting temperatures of ~723 °C, 462 °C, and 253 °C, respectively. This suggests that the earlier introduction of the melt phase may enhance the final density of the sintered phase, even when the precursors are mostly reacted by the sintering step. In all, it seems that the composition has an important role in defining the final density in pressure-free sintering and densification and given the flexibility of the composition in achieving phase purity and bulk conductivity, it may be beneficial to focus on the Li concentrations when pursuing sufficient density of the electrolyte.

4.4. Processing Flexibility and the Composition-Structure Relationship

To emphasize the complexity of the processing matrix on the resulting conductivity of LLZO, the samples with the highest conductivities are again examined. Even though they all reach >0.5

mS cm^{-1}, which is among the highest reported conductivities for LLZO-Al, they were all processed differently. The first sample had 15 wt.% excess Li_2CO_3 added in two stages in the synthesis process, then hot-pressed to form LLZO-Al0.17 with 7.22 mol Li and cubic phase stability with some pyrochlore secondary phase. The second sample had 15 mol% excess $LiNO_3$ added at the start of the synthesis process, then was sintered in mother powder to form LLZO-Al0.07 with 6.83 mol Li and cubic phase stability. The third sample had 15 wt.% Li_2CO_3 excess added at the start of the synthesis process, then was sintered without mother powder to form LLZO-Al0.06 with 6.12 mol Li and mixed cubic and tetragonal phase stability. The fourth sample had 15 wt.% Li_2CO_3 excess added in two steps, then was sintered in mother powder to form LLZO-Al0.17 with 6.70 mol Li and cubic phase stability. The fifth sample above 0.5 mS cm^{-1} had 15 wt.% Li_2CO_3 excess added in two steps, then was sintered in mother powder to form LLZO-Al0.23 with 6.86 mol Li and cubic phase stability.

Generally, when looking across these highest conductivity (>0.5 mS cm^{-1}) samples in contrast to the lowest conductivity samples (<0.1 mS cm^{-1}), it appears that the maximum bulk conductivity is achieved when a balance of charge carriers, vacancy concentration, and cubic phase stability is reached. This is achieved through sufficient Al doping (>0.16 mol Al) combined with a Li concentration range of 6.70-6.85 mol Li, leading to optimized structures for maximized Li conduction in LLZO-Al by increasing charge carrier concentration, Li-Li neighbor interactions, and vacancy concentration. This balance is schematically illustrated by the blue curves, axis, and structures in Figure 13. At lower Li concentrations and a sufficient concentration of Al, the bulk conductivity is lower due to the decreased number of Li ion charge carriers and corresponding decrease in Li-Li interactions as shown in the bottom left schematic. At high Li concentrations,

there are an insufficient number of vacancies in the Li ion sublattice, decreasing the overall conductivity as shown in the top left schematic by the small number of vacancies available for conduction. At Li ion concentrations between 6.70-6.85 mol Li and >0.16 mol Al, there is a balance of Li ion charge carriers, Li-Li interactions, and vacancies, leading to heightened conductivities, as schematically shown by the increased Li ion conducting arrows in the top right structure in Figure 13. In the cases where the Al or Li concentration are outside of this ideal range and a high bulk conductivity is still achieved (i.e., the $LiNO_3$ precursor sample and the 15/0 Li addition sample), pronounced losses of Zr and/or La are observed during the first calcination. These increased Zr losses are also observed in the LLZO-Al0.17 and LLZO-Al0.23 samples as compared to the LLZO-Al0.13 sample (nominally the LLZO-Al0.25, LLZO-Al0.35, and LLZO-Al0.15 samples, respectively). These increased Zr (and also La) losses during the initial reaction from precursors to LLZO may impact the framework structure, i.e. Zr vacancies may lead to changes in the M-O bond length, bottleneck size, and Li-Li site distances, all of which appear to favorably affect the bulk conductivity of the LLZO. This increase in conductivity with early Zr losses is shown schematically by the green axes, curve, and structures in Figure 13. Overall, the optimal compositions for high bulk conductivity generally balance cubic phase stability, high Li concentrations, and Li vacancies, though they also appear to be impacted by the losses of framework structure ions during processing.

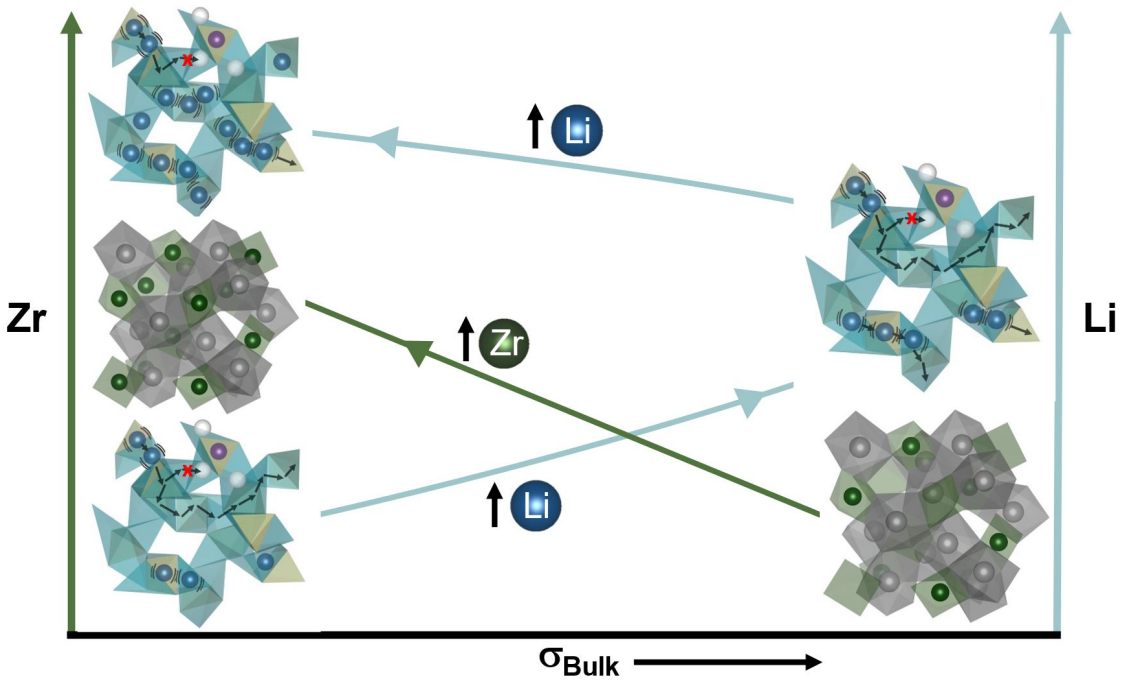

Figure 13. Schematic of potential structural contributions to conductivity. Zr (left) and Li (right) compositions as a function of bulk conductivity. Blue curve and axis correspond to the relationship between Li concentration and bulk conductivity. Green lines correspond to the relationship between Zr concentration and conductivity. Structures shown are schematics of the structure at that relative composition related to the Li ions/vacancies in the sublattice structure (blue structures) and Zr ions/vacancies in the framework structure (green structure). Blue spheres are Li ions, white spheres are trapped Li vacancies, purple spheres are Al ions. Arrows in the schematics illustrate Li ion conduction paths and parentheses indicate nearest neighbor interactions that lead to low activation energy motion. Red "x"s indicate paths blocked by the existence of Al and trapped vacancies. Green spheres are Zr ions and grey spheres are La ions.

5. Conclusions

In this work, we synthesized several series of LLZO-Al samples to discern the overall effects of composition and processing on the final phase purity, conductivity, and density. During calcination and sintering, we found that Li losses were limited to an average of ~0.6 mol Li while unexpected Al, Zr, and La losses were occurring, likely through Li-assisted or intermediary phase-assisted diffusion to the MgO crucible. The magnitude of the Al losses defined the phase purity of the samples, with samples <~0.06 mol Al exhibiting tetragonal phase stability, which is much a lower Al concentration than typically reported. Additionally, it was found that the Li melt phase was likely essential in the incorporation of Al into the LLZO and stabilization of a dense, high conductivity, cubic LLZO. While the Al composition was critical in defining the cubic phase stability, the cubic LLZO can be stabilized with a wide range of Li concentrations (6.08 mol to 7.61 mol Li). This wide compositional window for cubic LLZO brings to light the compositional flexibility of the cubic LLZO structure. Using impedance spectroscopy, we show that this flexibility in phase purity can also be expanded to the bulk conductivity, where Li composition, Al composition, and phase purity do not have clear individual roles in defining the conductivity. This flexibility and the confluence of several parameters, such as composition, precursors, Li addition timing, and density, can lead to multiple successful processing routes for achieving ≥0.7 mS cm^{-1}. While previous works tended to focus on one processing parameter at a time, the simultaneous exploration and aggregation of multiple variables reveals the wide compositional flexibility of the cubic phase and highlights the ability of a variety of successful processing paths to result in high conductivity garnet.

These findings allow for a greater understanding of the origins of the variable results achieved in past findings, encouraging future works to use compositional analysis to fully understand the

effects of processing on final electrochemical properties. Additionally, the demonstrated ability to achieve high conductivity through multiple paths opens up the design principles in achieving high conductivity LLZO to encompass a wide variety of processing parameters, compositions, and phases. The heightened Li compositions also encourage future work to gain a greater understanding of the mechanisms for cubic phase stability, especially as the expected vacancies present due to doping are below that expected for cubic phase stability based on previous works.

6. Supporting Information

The Supporting Information is available free of charge.

Composition as a function of processing step for all samples; bulk conductivity, density, phase purity, and lattice parameters for all densified samples; Rietveld fit for majority t-LLZO sample; lattice parameters as a function of Al and Li concentration; XRD of MgO crucible.

7. Acknowledgements

A.C.M would like to thank Jeffrey Einkauf and Diana Stamberga in Oak Ridge National Laboratory's Chemical Separations Group for repeated access to the ICP used in this work. This material is based upon work supported by the U.S. Department of Energy, Office of Science, Office of Workforce Development for Teachers and Scientists, Office of Science Graduate Student Research (SCGSR) program. The SCGSR program is administered by the Oak Ridge Institute for Science and Education for the DOE under contract number DE-SC0014664. A.C.M. would like to thank the Rackham Graduate School at the University of Michigan for support through the Rackham Pre-Doctoral Fellowship. A portion of this work (materials synthesis, ICP, EIS, XRD, and data analysis) was performed at the Oak Ridge National Laboratory (G.M.V., R.L.S., A.L.M,

A.C.M.) and supported by U.S. Department of Energy's Vehicle Technologies Office under the US-Germany Consortium Project, directed by Tien Duong. This manuscript has been authored in part by UT-Battelle, LLC, under contract DEAC05-00OR22725 with the U.S. Department of Energy (DOE). The publisher, by accepting the article for publication, acknowledges that the U.S. government retains a nonexclusive, paid-up, irrevocable, worldwide license to publish or reproduce the published form of this manuscript, or allow others to do so, for U.S. government purposes. The DOE will provide public access to these results of federally sponsored research in accordance with the DOE Public Access Plan (http://energy.gov/downloads/doepublic-accessplan).

8. References

(1) Han, G.; Kinzer, B.; Garcia-Mendez, R.; Choe, H.; Wolfenstine, J.; Sakamoto, J. Correlating the Effect of Dopant Type (Al, Ga, Ta) on the Mechanical and Electrical Properties of Hot-Pressed Li-Garnet Electrolyte. *J. Eur. Ceram. Soc.* **2020**, *40* (5), 1999–2006. https://doi.org/10.1016/j.jeurceramsoc.2019.12.054.

(2) Ma, C.; Cheng, Y.; Yin, K.; Luo, J.; Sharafi, A.; Sakamoto, J.; Li, J.; More, K. L.; Dudney, N. J.; Chi, M. Interfacial Stability of Li Metal–Solid Electrolyte Elucidated via in Situ Electron Microscopy. *Nano Lett.* **2016**, *16* (11), 7030–7036. https://doi.org/10.1021/acs.nanolett.6b03223.

(3) Shimonishi, Y.; Toda, A.; Zhang, T.; Hirano, A.; Imanishi, N.; Yamamoto, O.; Takeda, Y. Synthesis of Garnet-Type Li7−xLa3Zr2O12−1/2x and Its Stability in Aqueous Solutions. *Solid State Ion.* **2011**, *183* (1), 48–53. https://doi.org/10.1016/j.ssi.2010.12.010.

(4) Kokal, I.; Somer, M.; Notten, P. H. L.; Hintzen, H. T. Sol–Gel Synthesis and Lithium Ion Conductivity of Li7La3Zr2O12 with Garnet-Related Type Structure. *Solid State Ion.* **2011**, *185* (1), 42–46. https://doi.org/10.1016/j.ssi.2011.01.002.

(5) Jin, Y.; McGinn, P. J. Al-Doped Li7La3Zr2O12 Synthesized by a Polymerized Complex Method. *J. Power Sources* **2011**, *196* (20), 8683–8687. https://doi.org/10.1016/j.jpowsour.2011.05.065.

(6) Afyon, S.; Krumeich, F.; M. Rupp, J. L. A Shortcut to Garnet-Type Fast Li-Ion Conductors for All-Solid State Batteries. *J. Mater. Chem. A* **2015**, *3* (36), 18636–18648. https://doi.org/10.1039/C5TA03239C.

(7) Dhivya, L.; Karthik, K.; Ramakumar, S.; Murugan, R. Facile Synthesis of High Lithium Ion Conductive Cubic Phase Lithium Garnets for Electrochemical Energy Storage Devices. *RSC Adv.* **2015**, *5* (116), 96042–96051. https://doi.org/10.1039/C5RA18543B.

(8) Richerson, D. W.; Lee, W. E. *Modern Ceramic Engineering*, 4th ed.; CRC Press, Taylor and Francis Group, 2018.

(9) Geiger, C. A.; Alekseev, E.; Lazic, B.; Fisch, M.; Armbruster, T.; Langner, R.; Fechtelkord, M.; Kim, N.; Pettke, T.; Weppner, W. Crystal Chemistry and Stability of "Li7La3Zr2O12" Garnet: A Fast Lithium-Ion Conductor. *Inorg. Chem.* **2011**, *50* (3), 1089–1097. https://doi.org/10.1021/ic101914e.
(10) Rangasamy, E.; Wolfenstine, J.; Sakamoto, J. The Role of Al and Li Concentration on the Formation of Cubic Garnet Solid Electrolyte of Nominal Composition Li7La3Zr2O12. *Solid State Ion.* **2012**, *206*, 28–32. https://doi.org/10.1016/j.ssi.2011.10.022.
(11) Murugan, R.; Thangadurai, V.; Weppner, W. Fast Lithium Ion Conduction in Garnet-Type $Li_7La_3Zr_2O_{12}$. *Angew. Chem. Int. Ed.* **2007**, *46* (41), 7778–7781. https://doi.org/10.1002/anie.200701144.
(12) Raju, M. M.; Altayran, F.; Johnson, M.; Wang, D.; Zhang, Q. Crystal Structure and Preparation of Li7La3Zr2O12 (LLZO) Solid-State Electrolyte and Doping Impacts on the Conductivity: An Overview. *Electrochem* **2021**, *2* (3), 390–414. https://doi.org/10.3390/electrochem2030026.
(13) Li, Y.; Cao, Y.; Guo, X. Influence of Lithium Oxide Additives on Densification and Ionic Conductivity of Garnet-Type Li6.75La3Zr1.75Ta0.25O12 Solid Electrolytes. *Solid State Ion.* **2013**, *253*, 76–80. https://doi.org/10.1016/j.ssi.2013.09.005.
(14) Janani, N.; Deviannapoorani, C.; Dhivya, L.; Murugan, R. Influence of Sintering Additives on Densification and Li+ Conductivity of Al Doped Li7La3Zr2O12 Lithium Garnet. *RSC Adv.* **2014**, *4* (93), 51228–51238. https://doi.org/10.1039/C4RA08674K.
(15) Zheng, C.; Su, J.; Song, Z.; Xiu, T.; Jin, J.; Badding, M. E.; Wen, Z. Improvement of Density and Electrochemical Performance of Garnet-Type Li7La3Zr2O12 for Solid-State Lithium Metal Batteries Enabled by W and Ta Co-Doping Strategy. *Mater. Today Energy* **2022**, *27*, 101034. https://doi.org/10.1016/j.mtener.2022.101034.
(16) Zhang, C.; Hu, X.; Nie, Z.; Wu, C.; Zheng, N.; Chen, S.; Yang, Y.; Wei, R.; Yu, J.; Yang, N.; Yu, Y.; Liu, W. High-Performance Ta-Doped Li7La3Zr2O12 Garnet Oxides with AlN Additive. *J. Adv. Ceram.* **2022**, *11* (10), 1530–1541. https://doi.org/10.1007/s40145-022-0626-y.
(17) Buschmann, H.; Dölle, J.; Berendts, S.; Kuhn, A.; Bottke, P.; Wilkening, M.; Heitjans, P.; Senyshyn, A.; Ehrenberg, H.; Lotnyk, A.; Duppel, V.; Kienle, L.; Janek, J. Structure and Dynamics of the Fast Lithium Ion Conductor "Li 7 La 3 Zr 2 O 12 ." *Phys. Chem. Chem. Phys.* **2011**, *13* (43), 19378–19392. https://doi.org/10.1039/C1CP22108F.
(18) Bernstein, N.; Johannes, M. D.; Hoang, K. Origin of the Structural Phase Transition in ${\mathrm{Li}}_{7}{\mathrm{La}}_{3}{\mathrm{Zr}}_{2}{\mathrm{O}}_{12}$. *Phys. Rev. Lett.* **2012**, *109* (20), 205702. https://doi.org/10.1103/PhysRevLett.109.205702.
(19) Thompson, T.; Wolfenstine, J.; L. Allen, J.; Johannes, M.; Huq, A.; N. David, I.; Sakamoto, J. Tetragonal vs. Cubic Phase Stability in Al – Free Ta Doped Li 7 La 3 Zr 2 O 12 (LLZO). *J. Mater. Chem. A* **2014**, *2* (33), 13431–13436. https://doi.org/10.1039/C4TA02099E.
(20) Xiang, X.; Chen, F.; Shen, Q.; Zhang, L.; Chen, C. Effect of the Lithium Ion Concentration on the Lithium Ion Conductivity of Ga-Doped LLZO. *Mater. Res. Express* **2019**, *6* (8), 085546. https://doi.org/10.1088/2053-1591/ab2799.
(21) Limpert, M. A.; Atwater, T. B.; Hamann, T.; Godbey, G. L.; Hitz, G. T.; McOwen, D. W.; Wachsman, E. D. Achieving Desired Lithium Concentration in Garnet Solid Electrolytes; Processing Impacts on Physical and Electrochemical Properties. *Chem. Mater.* **2022**, *34* (21), 9468–9478. https://doi.org/10.1021/acs.chemmater.2c01915.

(22) Xia, W.; Xu, B.; Duan, H.; Tang, X.; Guo, Y.; Kang, H.; Li, H.; Liu, H. Reaction Mechanisms of Lithium Garnet Pellets in Ambient Air: The Effect of Humidity and CO2. *J. Am. Ceram. Soc.* **2017**, *100* (7), 2832–2839. https://doi.org/10.1111/jace.14865.
(23) Sudo, R.; Nakata, Y.; Ishiguro, K.; Matsui, M.; Hirano, A.; Takeda, Y.; Yamamoto, O.; Imanishi, N. Interface Behavior between Garnet-Type Lithium-Conducting Solid Electrolyte and Lithium Metal. *Solid State Ion.* **2014**, *262*, 151–154. https://doi.org/10.1016/j.ssi.2013.09.024.
(24) Zhuang, L.; Huang, X.; Lu, Y.; Tang, J.; Zhou, Y.; Ao, X.; Yang, Y.; Tian, B. Phase Transformation and Grain-Boundary Segregation in Al-Doped Li7La3Zr2O12 Ceramics. *Ceram. Int.* **2021**. https://doi.org/10.1016/j.ceramint.2021.04.295.
(25) Düvel, A.; Kuhn, A.; Robben, L.; Wilkening, M.; Heitjans, P. Mechanosynthesis of Solid Electrolytes: Preparation, Characterization, and Li Ion Transport Properties of Garnet-Type Al-Doped Li7La3Zr2O12 Crystallizing with Cubic Symmetry. *J. Phys. Chem. C* **2012**, *116* (29), 15192–15202. https://doi.org/10.1021/jp301193r.
(26) Parascos, K.; Watts, J. L.; Alarco, J. A.; Chen, Y.; Talbot, P. C. Optimizing Li+ Transport in Li7La3Zr2O12 Solid Electrolytes. *Ceram. Int.* **2023**. https://doi.org/10.1016/j.ceramint.2023.04.136.
(27) Moy, A. C.; Manjón-Sanz, A.; Caracciolo, T. C.; Lobanov, M. V.; Veith, G. M.; Sakamoto, J. Effects of Al Concentration on the Structure and Conductivity of Lithium Lanthanum Zirconium Oxide. *J. Mater. Chem. A* **2024**, *12* (41), 28193–28210. https://doi.org/10.1039/D4TA04862H.
(28) Moy, A. C.; Häuschen, G.; Fattakhova-Rohlfing, D.; Wolfenstine, J. B.; Finsterbusch, M.; Sakamoto, J. The Effects of Aluminum Concentration on the Microstructural and Electrochemical Properties of Lithium Lanthanum Zirconium Oxide. *J. Mater. Chem. A* **2022**. https://doi.org/10.1039/D2TA03676B.
(29) Vema, S.; Berge, A. H.; Nagendran, S.; Grey, C. P. Clarifying the Dopant Local Structure and Effect on Ionic Conductivity in Garnet Solid-State Electrolytes for Lithium-Ion Batteries. *Chem. Mater.* **2023**, *35* (22), 9632–9646. https://doi.org/10.1021/acs.chemmater.3c01831.
(30) Huang, X.; Lu, Y.; Song, Z.; Rui, K.; Wang, Q.; Xiu, T.; Badding, M. E.; Wen, Z. Manipulating Li2O Atmosphere for Sintering Dense Li7La3Zr2O12 Solid Electrolyte. *Energy Storage Mater.* **2019**, *22*, 207–217. https://doi.org/10.1016/j.ensm.2019.01.018.
(31) Heywood, S.; Lessmeier, M.; Driscoll, D.; Sofie, S. Tailoring Solid-State Synthesis Routes for High Confidence Production of Phase Pure, Low Impedance Al-LLZO. *J. Am. Ceram. Soc.* **2023**, *106* (5), 2786–2796. https://doi.org/10.1111/jace.18994.
(32) Wang, C.; Ping, W.; Bai, Q.; Cui, H.; Hensleigh, R.; Wang, R.; Brozena, A. H.; Xu, Z.; Dai, J.; Pei, Y.; Zheng, C.; Pastel, G.; Gao, J.; Wang, X.; Wang, H.; Zhao, J.-C.; Yang, B.; Zheng, X. (Rayne); Luo, J.; Mo, Y.; Dunn, B.; Hu, L. A General Method to Synthesize and Sinter Bulk Ceramics in Seconds. *Science* **2020**, *368* (6490), 521–526. https://doi.org/10.1126/science.aaz7681.
(33) Liu, K.; Ma, J.-T.; Wang, C.-A. Excess Lithium Salt Functions More than Compensating for Lithium Loss When Synthesizing Li6.5La3Ta0.5Zr1.5O12 in Alumina Crucible. *J. Power Sources* **2014**, *260*, 109–114. https://doi.org/10.1016/j.jpowsour.2014.02.065.
(34) Schwab, C.; Häuschen, G.; Mann, M.; Roitzheim, C.; Guillon, O.; Fattakhova-Rohlfing, D.; Finsterbusch, M. Towards Economic Processing of High Performance Garnets – Case

Study on Zero Li Excess Ga-Substituted LLZO. *J. Mater. Chem. A* **2023**, *11* (11), 5670–5680. https://doi.org/10.1039/D2TA09250F.
(35) Zhang, Y.; Chen, F.; Tu, R.; Shen, Q.; Zhang, X.; Zhang, L. Effect of Lithium Ion Concentration on the Microstructure Evolution and Its Association with the Ionic Conductivity of Cubic Garnet-Type Nominal Li7Al0.25La3Zr2O12 Solid Electrolytes. *Solid State Ion.* **2016**, *284*, 53–60. https://doi.org/10.1016/j.ssi.2015.11.014.
(36) Ashuri, M.; Golmohammad, M.; Soleimany Mehranjani, A.; Faghihi Sani, M. Al-Doped Li7La3Zr2O12 Garnet-Type Solid Electrolytes for Solid-State Li-Ion Batteries. *J. Mater. Sci. Mater. Electron.* **2021**, *32* (5), 6369–6378. https://doi.org/10.1007/s10854-021-05353-3.
(37) Cheng, L.; Sun Park, J.; Hou, H.; Zorba, V.; Chen, G.; Richardson, T.; Cabana, J.; Russo, R.; Doeff, M. Effect of Microstructure and Surface Impurity Segregation on the Electrical and Electrochemical Properties of Dense Al-Substituted Li 7 La 3 Zr 2 O 12. *J. Mater. Chem. A* **2014**, *2* (1), 172–181. https://doi.org/10.1039/C3TA13999A.
(38) Huang, X.; Song, Z.; Xiu, T.; Badding, M. E.; Wen, Z. Searching for Low-Cost LixMOy Compounds for Compensating Li-Loss in Sintering of Li-Garnet Solid Electrolyte. *J. Materiomics* **2019**, *5* (2), 221–228. https://doi.org/10.1016/j.jmat.2018.09.004.
(39) Baek, S.-W.; Lee, J.-M.; Kim, T. Y.; Song, M.-S.; Park, Y. Garnet Related Lithium Ion Conductor Processed by Spark Plasma Sintering for All Solid State Batteries. *J. Power Sources* **2014**, *249*, 197–206. https://doi.org/10.1016/j.jpowsour.2013.10.089.
(40) Suzuki, Y.; Kami, K.; Watanabe, K.; Watanabe, A.; Saito, N.; Ohnishi, T.; Takada, K.; Sudo, R.; Imanishi, N. Transparent Cubic Garnet-Type Solid Electrolyte of Al2O3-Doped Li7La3Zr2O12. *Solid State Ion.* **2015**, *278*, 172–176. https://doi.org/10.1016/j.ssi.2015.06.009.
(41) Zhang, Y.; Chen, F.; Tu, R.; Shen, Q.; Zhang, L. Field Assisted Sintering of Dense Al-Substituted Cubic Phase Li7La3Zr2O12 Solid Electrolytes. *J. Power Sources* **2014**, *268*, 960–964. https://doi.org/10.1016/j.jpowsour.2014.03.148.
(42) Dermenci, K. B.; Turan, S. Achieving High Performance for Aluminum Stabilized Li7La3Zr2O12 Solid Electrolytes for All Solid-State Li-Ion Batteries: A Thermodynamic Point of View. *Int. J. Energy Res.* **2019**, *43* (1), 141–149. https://doi.org/10.1002/er.4203.
(43) Hitz, G. T.; Wachsman, E. D.; Thangadurai, V. Highly Li-Stuffed Garnet-Type Li7+xLa3Zr2-xYxO12. *J. Electrochem. Soc.* **2013**, *160* (8), A1248. https://doi.org/10.1149/2.088308jes.
(44) Rietveld, H. M. A Profile Refinement Method for Nuclear and Magnetic Structures. *J. Appl. Crystallogr.* **1969**, *2* (2), 65–71. https://doi.org/10.1107/S0021889869006558.
(45) Coelho, A. A.; Evans, J.; Evans, I.; Kern, A.; Parsons, S. The TOPAS Symbolic Computation System. *Powder Diffr.* **2011**, *26* (S1), S22–S25. https://doi.org/10.1154/1.3661087.
(46) Dong, B.; Driscoll, L. L.; Stockham, M. P.; Kendrick, E.; Slater, P. R. Low Temperature Synthesis of Garnet Solid State Electrolytes: Implications on Aluminium Incorporation in Li7La3Zr2O12. *Solid State Ion.* **2020**, *350*, 115317. https://doi.org/10.1016/j.ssi.2020.115317.
(47) Dong, B.; Yeandel, S. R.; Goddard, P.; Slater, P. R. Combined Experimental and Computational Study of Ce-Doped La3Zr2Li7O12 Garnet Solid-State Electrolyte. *Chem. Mater.* **2020**, *32* (1), 215–223. https://doi.org/10.1021/acs.chemmater.9b03526.

(48) Yastrebtsev, A. A.; Popov, V. V.; Menushenkov, A. P.; Beskrovnyi, A. I.; Neov, D. S.; Shchetinin, I. V.; Ponkratov, K. V. Comparative Neutron and X-Ray Diffraction Analysis of Anionic and Cationic Ordering in Rare-Earth Zirconates (*Ln* = La, Nd, Tb, Yb, Y). *J. Alloys Compd.* **2020**, *832*, 154863. https://doi.org/10.1016/j.jallcom.2020.154863.
(49) Heiba, Z.; El-Sayed, K. Structural and Anisotropic Thermal Expansion Correlation of Li2ZrO3 at Different Temperatures. *J. Appl. Crystallogr.* **2002**, *35* (5), 634–636. https://doi.org/10.1107/S0021889802011214.
(50) Lehnert, H.; Boysen, H.; Schneider, J.; Frey, F.; Hohlwein, D.; Radaelli, P.; Ehrenberg, H. A Powder Diffraction Study of the Phase Transition in LaAlO3. *Z. Für Krist. - Cryst. Mater.* **2000**, *215* (9), 536–541. https://doi.org/10.1524/zkri.2000.215.9.536.
(51) Wiedemann, D.; Indris, S.; Meven, M.; Pedersen, B.; Boysen, H.; Uecker, R.; Heitjans, P.; Lerch, M. Single-Crystal Neutron Diffraction on γ-LiAlO2: Structure Determination and Estimation of Lithium Diffusion Pathway. *Z. Für Krist. - Cryst. Mater.* **2016**, *231* (3), 189–193. https://doi.org/10.1515/zkri-2015-1896.
(52) Malkowski, T. F.; Boeding, E. D.; Fattakhova-Rohlfing, D.; Wettengl, N.; Finsterbusch, M.; Veith, G. M. Digestion Processes and Elemental Analysis of Oxide and Sulfide Solid Electrolytes. *Ionics* **2022**, *28* (7), 3223–3231. https://doi.org/10.1007/s11581-022-04536-0.
(53) Smetaczek, S.; Wachter-Welzl, A.; Wagner, R.; Rettenwander, D.; Amthauer, G.; Andrejs, L.; Taibl, S.; Limbeck, A.; Fleig, J. Local Li-Ion Conductivity Changes within Al Stabilized Li 7 La 3 Zr 2 O 12 and Their Relationship to Three-Dimensional Variations of the Bulk Composition. *J. Mater. Chem. A* **2019**, *7* (12), 6818–6831. https://doi.org/10.1039/C9TA00356H.
(54) Thompson, T.; Sharafi, A.; Johannes, M. D.; Huq, A.; Allen, J. L.; Wolfenstine, J.; Sakamoto, J. A Tale of Two Sites: On Defining the Carrier Concentration in Garnet-Based Ionic Conductors for Advanced Li Batteries. *Adv. Energy Mater.* **2015**, *5* (11), 1500096. https://doi.org/10.1002/aenm.201500096.
(55) Miara, L. J.; Ong, S. P.; Mo, Y.; Richards, W. D.; Lee, J.-M.; Lee, H. S.; Ceder, G. Effect of Rb and Ta Doping on the Ionic Conductivity and Stability of the Garnet Li7+2x–y(La3–xRbx)(Zr2–yTay)O12 ($0 \leq x \leq 0.375$, $0 \leq y \leq 1$) Superionic Conductor: A First Principles Investigation. *Chem. Mater.* **2013**, *25* (15), 3048–3055. https://doi.org/10.1021/cm401232r.
(56) Awaka, J.; Takashima, A.; Kataoka, K.; Kijima, N.; Idemoto, Y.; Akimoto, J. Crystal Structure of Fast Lithium-Ion-Conducting Cubic $Li_7La_3Zr_2O_{12}$. *Chem. Lett.* **2011**, *40* (1), 60–62. https://doi.org/10.1246/cl.2011.60.
(57) Xie, H.; Alonso, J. A.; Li, Y.; Fernández-Díaz, M. T.; Goodenough, J. B. Lithium Distribution in Aluminum-Free Cubic Li7La3Zr2O12. *Chem. Mater.* **2011**, *23* (16), 3587–3589. https://doi.org/10.1021/cm201671k.
(58) Junio Samson, A.; Hofstetter, K.; Bag, S.; Thangadurai, V. A Bird's-Eye View of Li-Stuffed Garnet-Type Li 7 La 3 Zr 2 O 12 Ceramic Electrolytes for Advanced All-Solid-State Li Batteries. *Energy Environ. Sci.* **2019**, *12* (10), 2957–2975. https://doi.org/10.1039/C9EE01548E.
(59) Chen, F.; Xu, L.; Li, J.; Yang, Y.; Shen, Q. Effect of Bottleneck Size on Lithium Migration in Lithium Garnets Li7La3Zr2O12 (LLZO). *Ionics* **2020**, *26* (6), 3193–3198. https://doi.org/10.1007/s11581-020-03582-w.
(60) Xiang, X.; Chen, F.; Yang, W.; Yang, J.; Ma, X.; Chen, D.; Su, K.; Shen, Q.; Zhang, L. Dual Regulation of Li+ Migration of Li6.4La3Zr1.4M0.6O12 (M = Sb, Ta, Nb) by

Bottleneck Size and Bond Length of M−O. *J. Am. Ceram. Soc.* **2020**, *103* (4), 2483–2490. https://doi.org/10.1111/jace.16920.
(61) Zhang, Y.; Chen, F.; Li, J.; Zhang, L.; Gu, J.; Zhang, D.; Saito, K.; Guo, Q.; Luo, P.; Dong, S. Regulation Mechanism of Bottleneck Size on Li+ Migration Activation Energy in Garnet-Type Li7La3Zr2O12. *Electrochimica Acta* **2018**, *261*, 137–142. https://doi.org/10.1016/j.electacta.2017.12.133.
(62) Cook, L. P.; Plante, E. R.; Roth, R. S.; Hastie, J. W. *Phase Equilibria of Stored Chemical Energy Reactants.*; NATIONAL BUREAU OF STANDARDS GAITHERSBURG MD INORGANIC MATERIALS DIV, 1984. https://apps.dtic.mil/sti/citations/ADA146527 (accessed 2021-03-26).
(63) Kingery, W. D.; Bowen, H. K.; Uhlmann, D. R. *Introduction to Ceramics*, 2nd ed.; John Wiley & Sons: New York, NY, 1976.
(64) Chen, Y.; Rangasamy, E.; Cruz, C. R. dela; Liang, C.; An, K. A Study of Suppressed Formation of Low-Conductivity Phases in Doped Li7La3Zr2O12 Garnets by in Situ Neutron Diffraction. *J. Mater. Chem. A* **2015**, *3* (45), 22868–22876. https://doi.org/10.1039/C5TA04902D.
(65) Posch, P.; Lunghammer, S.; Berendts, S.; Ganschow, S.; Redhammer, G. J.; Wilkening, A.; Lerch, M.; Gadermaier, B.; Rettenwander, D.; Wilkening, H. M. R. Ion Dynamics in Al-Stabilized Li7La3Zr2O12 Single Crystals – Macroscopic Transport and the Elementary Steps of Ion Hopping. *Energy Storage Mater.* **2020**, *24*, 220–228. https://doi.org/10.1016/j.ensm.2019.08.017.
(66) Adams, S. Topological Control of Room Temperature Conductivity in Garnet-Type Solid Electrolytes. *Ionics* **2022**. https://doi.org/10.1007/s11581-022-04674-5.
(67) Chen, Y.; Rangasamy, E.; Liang, C.; An, K. Origin of High Li+ Conduction in Doped Li7La3Zr2O12 Garnets. *Chem. Mater.* **2015**, *27* (16), 5491–5494. https://doi.org/10.1021/acs.chemmater.5b02521.
(68) García Daza, F. A.; Bonilla, M. R.; Llordés, A.; Carrasco, J.; Akhmatskaya, E. Atomistic Insight into Ion Transport and Conductivity in Ga/Al-Substituted Li7La3Zr2O12 Solid Electrolytes. *ACS Appl. Mater. Interfaces* **2019**, *11* (1), 753–765. https://doi.org/10.1021/acsami.8b17217.
(69) Huang, X.; Lu, Y.; Guo, H.; Song, Z.; Xiu, T.; Badding, M. E.; Wen, Z. None-Mother-Powder Method to Prepare Dense Li-Garnet Solid Electrolytes with High Critical Current Density. *ACS Appl. Energy Mater.* **2018**, *1* (10), 5355–5365. https://doi.org/10.1021/acsaem.8b00976.
(70) Doux, J.-M.; Yang, Y.; S. Tan, D. H.; Nguyen, H.; A. Wu, E.; Wang, X.; Banerjee, A.; Shirley Meng, Y. Pressure Effects on Sulfide Electrolytes for All Solid-State Batteries. *J. Mater. Chem. A* **2020**, *8* (10), 5049–5055. https://doi.org/10.1039/C9TA12889A.

For Table of Contents Only

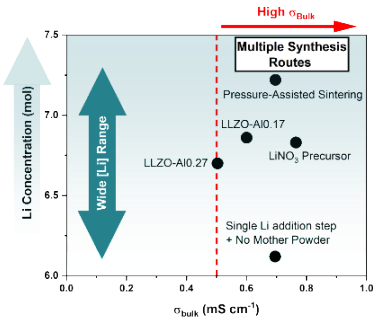
High σ_{Bulk}
Multiple Synthesis Routes
Pressure-Assisted Sintering
LLZO-Al0.17
$LiNO_3$ Precursor
LLZO-Al0.27
Single Li addition step + No Mother Powder
Wide [Li] Range
Li Concentration (mol)
7.5
7.0
6.5
6.0
0.0
0.2
0.4
0.6
0.8
1.0
σ_{bulk} (mS cm^{-1})